Geophysical and Astrophysical Fluid Dynamics
Vol. 00, No. 00, 00 Month 20xx, 1–28

Instability of two dimensional vortices with a peripheral ring

Raphael Ravasse†*, Jonathan Gula † and Xavier Carton †

† Univ Brest, CNRS, Ifremer, IRD, Laboratoire d'Océanographie Physique et Spatiale (LOPS), IUEM, 29280, Plouzané, France.

(*Received 00 Month 20xx; final version received 00 Month 20xx*)

We study the instability of piecewise-constant circular vortices with an accent put on like-signed and concentric core and annulus, in a two-dimensional incompressible fluid. Firstly, the linear instability of these vortices is studied. We determine the possible resonances between Rossby waves on the three vorticity fronts of the circular vortex and classify them with respect to the front positions and vorticity jumps. The wavenumber and growth rates of the most unstable normal-mode perturbations are also provided, when these parameters are varied. Secondly, we simulate the finite-amplitude evolution of these linearly unstable vortices using a numerical code of the nonlinear two-dimensional vorticity equation. It was shown that four main nonlinear regimes can occur: vortex core deformation, vortex core breaking, annulus breaking into a ring of vortices, and dipolar breaking of the whole structure. We then classify these regimes within the parameter space, and then describe possible turbulent evolutions of the initial circular vortex and explain the underlying physical mechanisms. We determine under which conditions vortex multipoles can be created and which shape they assume in a steady state, and present stable multipoles and give a simple criterion for this stability. These evolutions were contrasted with those previously obtained for oceanic vortices with a core and an opposite sign annulus. We show the essential role of like-signed vorticity regions, which often leads to spatial confinement of the vorticity end-states. Though highly idealized, our model results are compared with those of previous studies and with the observations of the Jupiter polar vortices.

1. Introduction

In planetary fluids, mesoscale and synoptic vortices are long-lived, horizontally recirculating fluid motions, with lifetimes much longer than their turnover periods (McWilliams 1991). In the Earth oceans, vortices are ubiquitous and are robust structures : they can live for months or even years (Richardson and Tychensky 1998). Oceanic vortices can drift far away from their formation region : deep vortices containing Mediterranean Water can cross half of the Atlantic Ocean westward (Carton 2001). Many oceanic vortices have a large heat and energy content that they retain and carry during their drift ; the turbulent heat transport at mid latitudes reaches 0.3-0.8 PW, a third to a half of the total heat transport across the oceans (Carli *et al.* 2023).

The stability of oceanic vortices has been the subject of many papers (e.g., Gent and McWilliams 1986, Flierl 1988, Dritschel 1988, Hua 1988a,b, Ford 1994, Dritschel and De la Torre Juárez 1996, Dewar and Killworth 1995, Sokolovskiy 1997, Dewar *et al.* 1999, Sokolovskiy and Verron 2000, Dritschel *et al.* 2005, Reinaud 2019). Many of these studies have considered idealized vorticity profiles to represent oceanic vortices. In particular, piecewise-constant and power-exponential vorticity profiles have often been used. These studies have shown that barotropic instability can affect vortices with profile steepness equal to (or larger than) that of Gaussian vortices (Ford 1994). During the nonlinear evolution of these unstable circular vortices, tripoles and quadrupoles can be formed and remain stable or metastable (Carton *et al.* 1989, Morel and Carton 1994). Dipolar breaking of strongly sheared

*Corresponding author. Email: raphael.ravasse@univ-brest.fr

vortices has also been observed (Carton and McWilliams 1989). In stratified rotating fluids (such as the atmosphere and oceans), baroclinic instability can affect surface-confined, or vertically contra-rotating, vortices (Dewar and Killworth 1995, Dewar *et al.* 1999, Baey and Carton 2002). The end-state of the baroclinically unstable vortices is either baroclinic dipoles (the so-called "hetons" (Hogg and Stommel 1985, Sokolovskiy and Verron 2000, Sokolovskiy 1997)), baroclinic tripoles (Corréard and Carton 1999, Sokolovskiy and Carton 2010, Kurakin *et al.* 2016) or vertically co- or contra-rotating elliptical vortices (Dewar and Killworth 1995, Carton and McWilliams 1996).

But vortices also exist on other planets (at least in the Solar System). The oldest known vortex in the Solar System is the Jupiter Great Red Spot, perhaps observed by Cassini (Cassini 1666), but known at least since 1831 (as reported by an observation by Hollow, noted by Clerke (1887)). It is an anticyclonic oval vortex of zonal dimension 16,000 km (half that of a century ago), lying at 22 degrees south of the Equator, and embedded in the zonal wind system of Jupiter. It is often accompanied by oval cyclones.
More recently, vortices have been observed by space probes at planetary poles. For Venus, the Venus Express mission (2006) revealed that the polar vortices on Venus have a double structure, unlike the mostly monopolar polar vortices on Earth (Svedhem *et al.* 2007). For Jupiter (Juno mission) and Saturn (Cassini mission), long-lived polygonal vortices, or vortex compounds, exist at their poles (Godfrey 1988, Sanchez-Lavega *et al.* 1993, Sánchez-Lavega *et al.* 2014, Ingersoll *et al.* 2022). At the North Pole of Jupiter, eight cyclonic vortices surround a central cyclone; at its South Pole, five peripheral vortices circle the central vortex. Their maximal (wind) velocity lies between 100 and 150 m/s at a radius of about 1000-1500 km from their center. The peripheral vortices are distant by about 8000 km from the North Pole and about 7000 km from the South pole.

Several studies proposed an explanation for the formation or the existence of these multipolar vortices as aggregates of drifting vortices, or as vortex crystals (Li *et al.* 2020, Gavriel and Kaspi 2021, Scarica *et al.* 2022, Siegelman *et al.* 2022). Other work has studied how the instability of an annular vortex can form a vortex multipole (Reinaud and Dritschel 2019), or a steadily rotating polygonal vortex (Rostami *et al.* 2017). In this paper, we complement their work in the context of two-dimensional flows, where parametric studies are easier. Indeed, the vertical structure of the polar vortices of giant gaseous planets is unknown, so that a 2D model is a natural setting for a parametric study of that type of vortices. At the end of the present paper, we propose a comparison of our results with those of previous studies. This paper also complements the Morel and Carton (1994) study which considered vorticity profiles more representative of Earth oceanic vortices.

In the following section, we detail the linear and nonlinear model equations and their numerical implementation. In section 3, the properties of the linear instability are given for such multi-front, circular vortices. In section 4, we present and analyze the various nonlinear regimes for the evolution of such perturbed vortices. Section 5 is devoted to the analysis of vortex multipoles formed by the instability of the circular vortex. Finally, we discuss our results, compare them with those of previous studies; conclusions and openings close this paper.

2. Model equations and numerical implementation

2.1. Model equations

In this paper, we study vortex stability in a two-dimensional incompressible fluid. The evolution of the fluid is governed by the conservation of vorticity (the curl of the horizontal velocity)

$$\partial_t \zeta + J(\psi, \zeta) = 0 \tag{1}$$

where $\zeta = \nabla^2 \psi$ is vorticity and ψ is the streamfunction. The Jacobian operator in polar coordinates is defined by

$$J(f,g) \;=\; \frac{1}{r}\,[\partial_r f\;\partial_\theta g \;-\; \partial_r g\;\partial_\theta f],$$

with $v_r = (-1/r)\;\partial_\theta \psi,\;\; v_\theta = \partial_r \psi$, the radial and tangential velocities.

In view of the polar vortices observations (Antuñano *et al.* 2019, Ingersoll *et al.* 2022), it is appropriate to define a radial profile of vorticity that is step-like, to retain only a few parameters for our vortex stability problem (and also to allow a comparison with Morel and Carton (1994) study).
Calling $\overline{\zeta}(r)$ the radial profile of vorticity for the circular vortex, we have

$$\overline{\zeta}(r) = 1, \quad r < 1 \quad \text{(core)} \tag{2}$$

$$\overline{\zeta}(r) = \omega_0, \quad 1 < r < r_0 \quad \text{(trough)} \tag{3}$$

$$\overline{\zeta}(r) = \omega_1, \quad r_0 < r < r_1 \quad \text{(annulus)} \tag{4}$$

$$\overline{\zeta}(r) = 0, \quad r > r_1 \quad \text{(exterior)} \tag{5}$$

This mean vorticity profile is shown in figure (1). This vortex has piecewise-constant vorticity, with three vorticity fronts: the inner, the intermediate, and the outer one. We call "core" the part of the vortex bounded by the inner contour. We call "annulus" the part of the vortex bounded by the intermediate and outer fronts. We call "trough" the region between the core and the annulus.

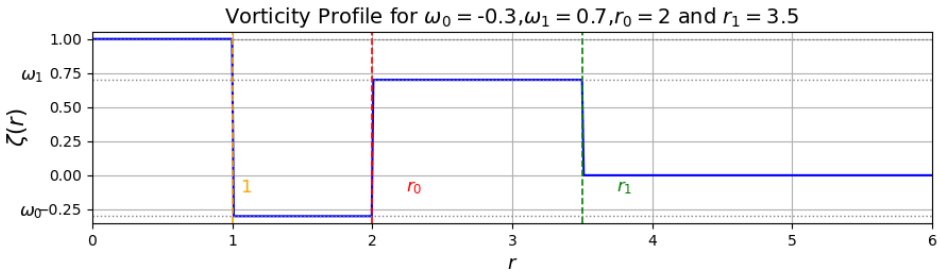

Figure 1. Radial vorticity profile of the circular vortex.

The associated stream-function $\overline{\psi}(r)$ and azimuthal velocity $\overline{V}(r)$ can easily be computed using their continuity at each vorticity front. Here, the annulus vorticity ω_1 is varied between 0.1 and 10. The trough vorticity ω_0 will either be negative, zero, or larger than unity to satisfy the Rayleigh criterion for barotropic instability.

2.2. Linear instability

Our aim is to determine under which conditions a perturbation with an angular mode l, comparable with the observed number of peripheral vortices at the Jupiter poles (e.g., $l = 5$ or $l = 8$), can grow on this circular vortex. We resort to normal mode theory to assess the stability of this vortex[1]. We perturb the radius of each vorticity front R_j from a constant value R_{0j} to one oscillating with the angle θ:

$$R_j(\theta, t) = R_{0j} + \ \epsilon \ \Re \ [a_j \ \exp(il(\theta - ct))] \tag{6}$$

where $R_{01} = 1, R_{02} = r_0, R_{03} = r_1$. Here ϵ is small, and $c = c_r + ic_i$ with c_r the perturbation phase speed and $\sigma = lc_i$ its growth rate. This vorticity front displacement is associated with a streamfunction perturbation

$$\psi'(r, \theta, t) = \ \epsilon \ \Re \ [\phi(r) \ \exp(il(\theta - ct))]$$

The vorticity equation (1) is linearized around the mean (circular) vortex flow to yield the Rayleigh equation:

$$[\overline{V}/r \ - c] \ \zeta' - \psi' \frac{d\overline{\zeta}}{dr} \ = \ 0. \tag{7}$$

Using the Rayleigh criterion for barotropic instability, we note that if $0 < \omega_1 < 1$ and $\omega_0 \in [\omega_1, 1]$, the vortex is linearly stable to normal mode perturbations.
In appendix A, we use an asymptotic expansion to determine whether the Rayleigh criterion is also sufficient in our case. The result is that it is not.

The theory of barotropic instability, considered as the growth of resonant Rossby waves on the vorticity fronts, indicates that :
- if $\omega_0 = 0$, $r_0 \simeq 1 + \epsilon$ and $r_1 \gg r_0$ the predominant resonance will occur between the inner and intermediate vorticity fronts. Conversely, with $r_1 \simeq r_0 \gg 1$, the predominant resonance will occur between the intermediate and outer vorticity fronts.
- if $\omega_0 < 0$ with ω_1 finite (e.g. unity), the velocity shear will be stronger in the trough, which will favor instability there. On the contrary, if $\omega_0 = 1 + \epsilon$ and ω_1 is much larger than unity, the shear will be stronger in the annulus (if it is narrow).

Coming back to the Rayleigh equation, note that, in each radial domain $(]R_j, R_k[)$, the gradient of mean vorticity is zero and so is the perturbation of relative vorticity. This leads to

$$\frac{d^2\phi}{dr^2} + \frac{1}{r} \ \frac{d\phi}{dr} - \frac{l^2}{r^2} \ \phi \ = \ 0 \tag{8}$$

leading to $\phi(r) = \alpha_j \ r^l + \beta_j \ r^{-l}$ in each radial domain. For finiteness of ψ', one has $\beta_1 = \alpha_4 = 0$. The continuity of ϕ at each vorticity front, and the integration of equation (2) around each mean vorticity front position r_{0j}, lead to a 3×3 system of linear equations which is solved by a matrix method (see details in section 3).

2.3. Nonlinear numerical model

The nonlinear vorticity equation (1) is solved using the Fluid2D package (Roullet 2025). Fluid2D is a Python-Fortran code for the simulation of two-dimensional incompressible flows. It can accomodate several equations (e.g. the vorticity equation and a temperature evolution equation). It is based on the resolution of dynamical equations with finite volumes. Time

[1]The growth of transient perturbations could be computed via the singular mode analysis; this is left for future work

stepping is done with a third order Runge Kutta scheme. In our experiments, the spatial (horizontal) grid has 128×128 nodes, and the time step is adapted from an initial guess of 0.2 model time units. For this model we used a 5-order upwinded interpolation, as explained in Roullet (2025). This scheme runs without any explicit dissipation.
To check the validity of our results, we ran identical simulations with a nonlinear pseudo-spectral code of the two-dimensional vorticity equation. We used a 256×256 horizontal resolution for this model. These simulations (not shown here) confirmed the results of the Fluid2D code.

In the Fluid2D model, the initialization is achieved using the circular vortex (equations 2-5), with vorticity fronts displaced by a 1% white noise perturbation.
The growth of the various modes of perturbation during the nonlinear evolution of the linearly unstable vortices is quantified via a Fourier analysis. We compute the amplitude of each mode (l) via :

$$A_l := \frac{1}{2\pi}\sqrt{\left(\int_0^{2\pi} \psi' \cos(l\theta)d\theta\right)^2 + \left(\int_0^{2\pi} \psi' \sin(l\theta)d\theta\right)^2}.$$

In particular, we checked that during the linear stage of the evolution, the most unstable mode grows at the rate indicated by linear theory.

3. Linear instability of vortices with a ring

3.1. Analytical calculations

To relate the coefficients α_j, β_j of ψ' with the radial displacements a_j, we apply the following conditions at each vorticity front :

- continuity of radial velocity : $[\frac{1}{r}\partial_\theta\psi]_r = 0$, which applies to the perturbation
- continuity of tangential velocity : $[\partial_r\psi]_r = 0$, which applies to both the mean flow and the perturbation
- kinematic equation of the front : $(\partial_t + \frac{1}{\overline{r}}\frac{\partial\overline{\psi}}{\partial r}\partial_\theta)\, r' = -\frac{1}{r}\partial_\theta\psi'$

The continuity of radial velocity simply gives $[\phi(r)] = 0$ (continuity of ϕ) as $\overline{\psi}$ doesn't depend on θ. This leads to the following three relations :

$$\begin{aligned}
\alpha_1 &= \alpha_2 + \beta_2, (\beta_1 = 0 \ \text{for non} - \text{divergence}),\\
\alpha_2 r_0^l + \beta_2 r_0^{-l} &= \alpha_3 r_0^l + \beta_3 r_0^{-l},\\
\alpha_3 r_1^l + \beta_3 r_1^{-l} &= \beta_4 r_1^{-l}, (\alpha_4 = 0 \ \text{for non} - \text{divergence}),
\end{aligned}$$

and we can then determine all coefficients with respect to α_2, β_2 and α_3 only :
$\alpha_1 = \alpha_2 + \beta_2$, $\beta_3 = \beta_2 + (\alpha_2 - \alpha_3)r_0^{2l}$ and $\beta_4 = \beta_3 + \alpha_3 r_1^{2l} = \beta_2 + (\alpha_2 - \alpha_3)r_0^{2l} + \alpha_3 r_1^{2l}$.

We apply a Taylor expansion to the continuity of tangential velocity :

$$\partial_r\psi(r) = \partial_r(\overline{\psi} + \varepsilon\psi')(\overline{r} + \varepsilon r') \tag{9}$$

$$\approx \partial_r\overline{\psi}(\overline{r}) + \varepsilon(r'\partial^2_{rr}\overline{\psi} + \partial_r\psi') \tag{10}$$

Then, we have $\left[r'\partial^2_{rr}\overline{\psi} + \partial_r\psi'\right]_r = 0$.

Inserting $r'_i = \eta_i e^{il(\theta - ct)}$ ($r' \in \{1, r_0, r_1\}$), we have :

$$\eta_j[\overline{\zeta}] + \left[\frac{d\phi}{dr}\right]_{r_j} = 0$$

We obtain three equations relating the radial displacements and the perturbation stream-function:

$$\eta_1 = \frac{-2l\beta_2}{\omega_0 - 1}$$
$$\eta_2 = \frac{2l}{\omega_0 - \omega_1}(\alpha_3 - \alpha_2) r_0^{l-1}$$
$$\eta_3 = -\frac{2l}{\omega_1} r_1^{l-1} \alpha_3$$

The linearized kinematic equation is

$$\left(\frac{\overline{V_\theta}}{\overline{r}} - c\right)\eta_j = -\frac{1}{r_j}\left(\alpha_j r_j^l + \beta_j r_j^{-l}\right).$$

Finally we can express the three kinematic equations under the form $A\boldsymbol{\eta} = c\boldsymbol{\eta}$ where $\boldsymbol{\eta} = (\eta_1, \eta_2, \eta_3)^T$.

We have the following matrix :

$$A = \begin{pmatrix} \frac{1}{2} - \frac{1-\omega_0}{2l} & \frac{r_0^{1-l}(\omega_1 - \omega_0)}{2l} & -\frac{r_1^{1-l}\omega_1}{2l} \\ -\frac{r_0^{-l-1}(1-\omega_0)}{2l} & \frac{\omega_0}{2} + \frac{1-\omega_0}{2r_0^2} + \frac{\omega_1 - \omega_0}{2l} & -(\frac{r_0}{r_1})^{l-1}\frac{\omega_1}{2l} \\ -\frac{1-\omega_0}{2lr_1^{l+1}} & \frac{1}{2l}(\frac{r_0}{r_1})^{l+1}(\omega_1 - \omega_0) & \frac{\omega_1}{2}(1 - \frac{1}{l}) + (\omega_0 - \omega_1)\frac{r_0^2}{2r_1^2} + \frac{1-\omega_0}{2r_1^2} \end{pmatrix} \tag{11}$$

To each eigenvector η corresponds an eigenvalue c in this diagonalization problem. The values of c can also be found by solving $det(A - cI_3) = 0$ (providing a third degree polynomial). These eigenvalues are obtained in a range of ω_0, ω_1, r_0, and r_1, and the maximum growth rate of the instability is computed as the maximum of $l|c_i|$ over a range of l (integer values)..

3.2. Vortex instability in the reference case

The study here is analogous and generalizes results obtained in Dritschel (1989). In this study, the author analyses evolution of a strip with different vorticity which corresponds to the interface between different layers in a shielded vortex. He also looks at the growth rates and studies how a vortex with different layers evolve in time.

Here we present the reference case, for which there is no vorticity in the trough. We study the maximal growth rates and the corresponding azimuthal wavenumbers, and interpret them as the resonance of Rossby waves on the vorticity fronts.

3.2.1. Growth rates and unstable waves for $\omega_0 = 0$, $\omega_1 = 1$

The maximal growth rates in the reference case are found in two regions of the parameter space : $r_0 \approx 1$ or $r_1 \approx r_0$ (Figure 2). As mentioned in our preliminary analysis, the first case corresponds to resonant inner and intermediate fronts and the second case to resonant intermediate and outer fronts, due to their relative proximity (the mean vorticity values being equal in the core and the annulus of the vortex). Physically, the area $r_1 < r_0$ is excluded.

When vorticity fronts are close, it is possible for short perturbations to grow on them. This is evident here in the large values of $l(\sim 10)$ in these two cases. On the contrary, longer waves become predominant when the trough and annulus are both wide, corresponding to distant vorticity fronts.

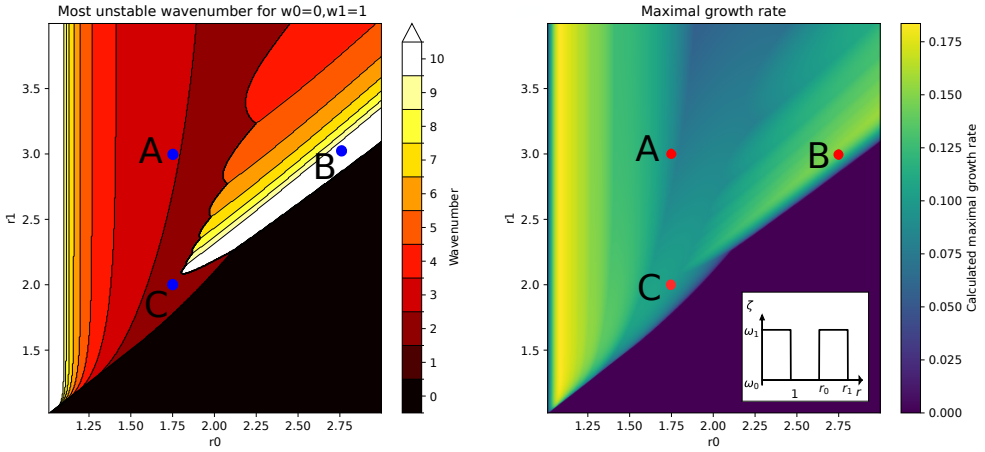

Figure 2. Instability for $\omega_0 = 0$ and $\omega_1 = 1$; left panel : most unstable mode; right panel : maximal growth rate over $l = 1 - 10$. Insert: radial profile of vorticity. Dots indicate the location of cases **A**, **B**, and **C** shown in Figures 3 and 4.

3.2.2. Wave resonance

The eigenvectors of the matrix (11) provide the spatial structure of the most unstable waves of perturbation. Since the vorticity is piecewise constant, they indicate which contours will be most disturbed (see figure 3).

Case **A** : $r_0 = 1{,}75$, $r_1 = 3$ Case **B** : $r_0 = 2{,}75$, $r_1 = 3$ Case **C** : $r_0 = 1{,}75$, $r_1 = 2$

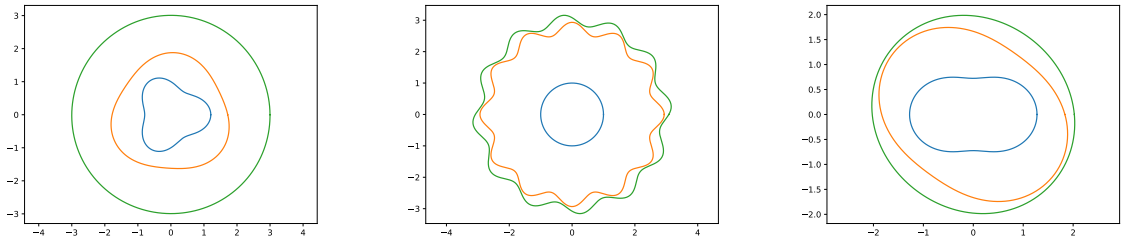

Figure 3. Vorticity contours of the most unstable linear eigenmodes for different (r_0, r_1) with $\omega_0 = 0$ and $\omega_1 = 1$. From left to right: Case A ($r_0 = 1.75, r_1 = 3$) with $l = 3$, Case B ($r_0 = 2.75, r_1 = 3$) with $l = 12$, and Case C ($r_0 = 1.75, r_1 = 2$) with $l = 2$.

For case **A**, the vorticity fronts are well separated. This allows for the growth of long-wave perturbations (here $l = 2, 3$) on the inner and intermediate vorticity fronts. On the contrary, for case **B**, the intermediate and outer fronts are very close to each other, thus favoring the growth of short-wave perturbations, here corresponding to a mode $l = 9$. For case **C**, where $l = 2$ is the most unstable mode, the contours are deformed into an ellipse, which has a large amplitude on the three vorticity contours.

Wave resonance can be explained by looking at the phase speeds and growth rates of the modes in figure 4. The growth rate is non-zero when two waves have identical phase speeds. This illustrates the interpretation of instability via wave resonance. In cases **A** and **B** we observe long- and short-wave instabilities, which are interactions between the inner and intermediate modes and the intermediate and outer mode, respectively. But in case **C**, we observe two different growth rate maxima for long and short wave perturbations.

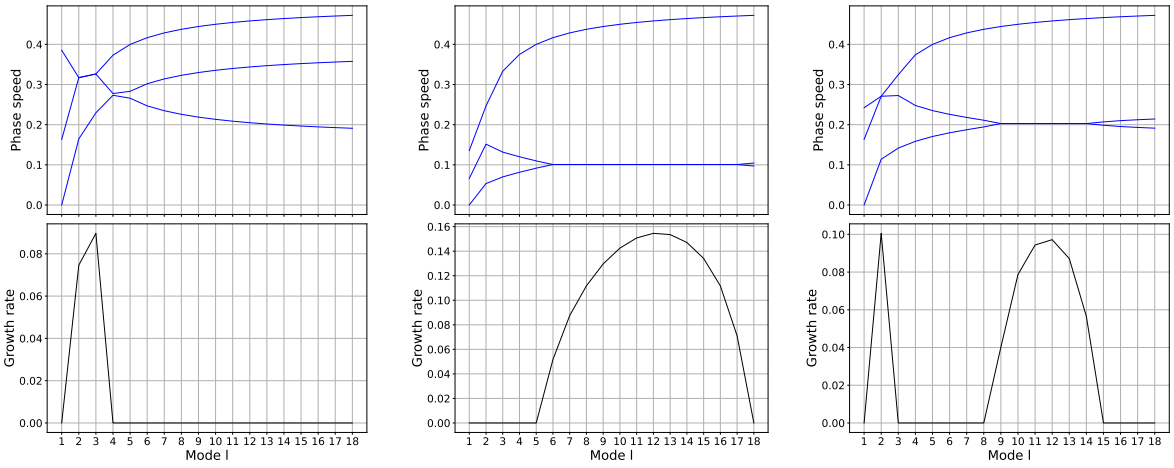

(a) Case **A**: $r_0 = 1.75$, $r_1 = 3$ (b) Case **B**: $r_0 = 2.75$, $r_1 = 3$ (c) Case **C**: $r_0 = 1.75$, $r_1 = 2$

Figure 4. Phase speeds (up) and growth rates (down) for different (r_0, r_1) with $\omega_0 = 0$ and $\omega_1 = 1$.

3.3. Sensitivity of linear instability to the relative amplitudes of mean vorticity

3.3.1. Case $\omega_0 = 0$, $\omega_1 = 0.1$

Keeping zero vorticity in the trough, we investigate the influence of small peripheral vorticity. This situation is shown in figure 5. As expected, the growth rates related to the resonance of waves between the intermediate and outer fronts are small. The preferred resonance occurs between Rossby waves on the inner and intermediate fronts. The consequences are that:
(1) growth rates decay strongly and vanish when the inner and intermediate fronts are too distant from each other;
(2) a change in r_1 does not influence the growth rates.

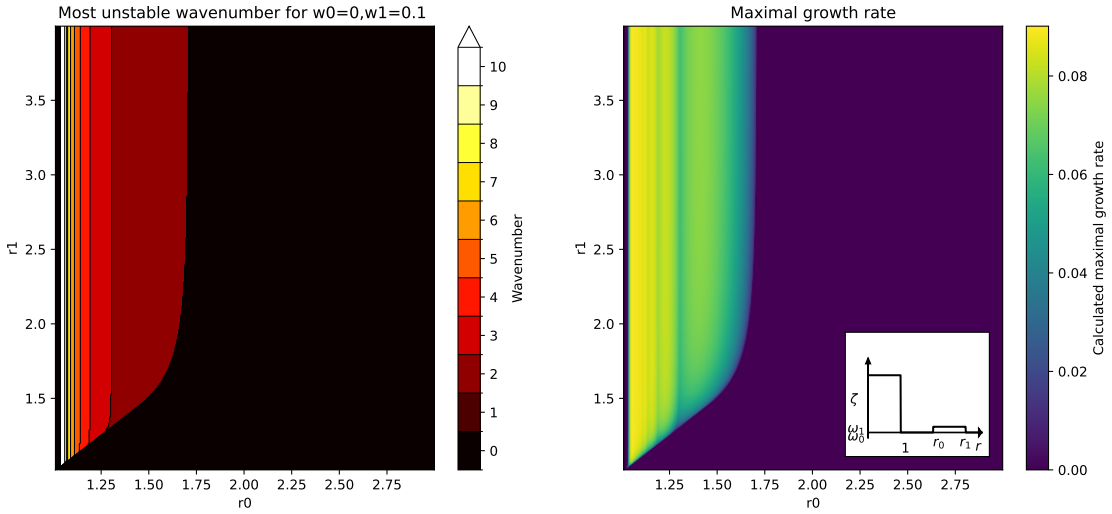

Figure 5. Instability for $\omega_0 = 0$ and $\omega_1 = 0.1$ left panels : most unstable wavenumber. right panels : growth rates. Insert: radial profile of mean vorticity.

3.3.2. Case $\omega_0 = 0$, $\omega_1 = 10$

Now, we consider the opposite situation where the peripheral vorticity is intense. The most unstable waves and their growth rates are shown in figure 6. This large peripheral vorticity

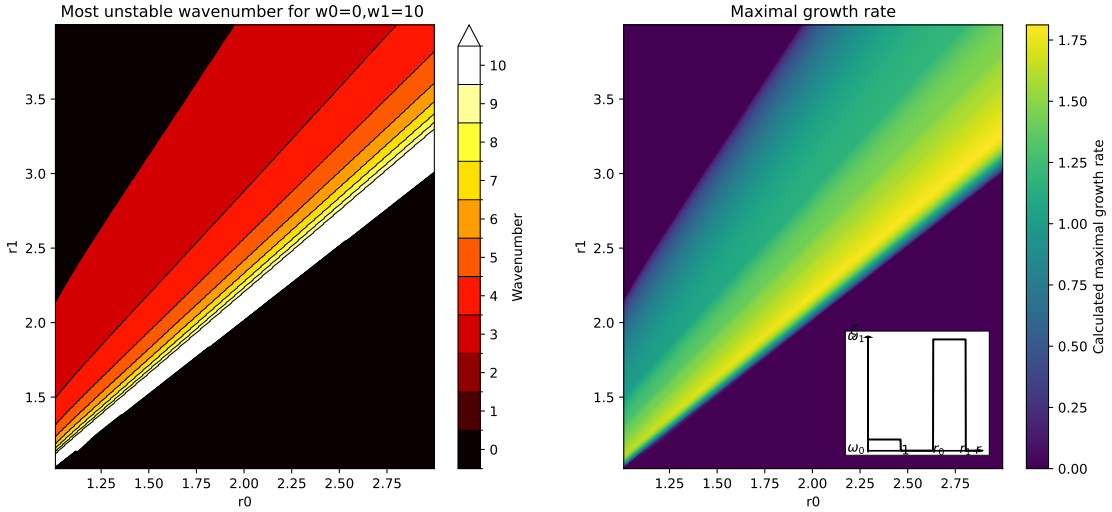

Figure 6. Instability for $\omega_0 = 0$ and $\omega_1 = 10$; left panel : most unstable mode. right panel : growth rates. Insert: radial profile of mean vorticity.

favors the resonance of the intermediate and outer frontal (Rossby) waves; their interaction with the Rossby wave on the inner front is much weaker. This is clearly manifested in the growth rates which are maximal for $r_0 \simeq r_1$, allowing the growth of short waves. When $r_1 > r_0$, longer waves become more unstable and eventually when $r_1 \gg r_0$, the flow is stable.

3.3.3. Case $\omega_0 = -0.5$, $\omega_1 = 1$

We now return to the reference case for the peripheral vorticity, with $\omega_1 = 1$, but allow for a negative mean vorticity in the trough. This corresponds to figure 7. The maps are very close to the reference case in terms of the most unstable wavenumber and resonances between waves. The only difference is that the growth rate values are larger due to the larger vorticity gradients at the inner and intermediate fronts.

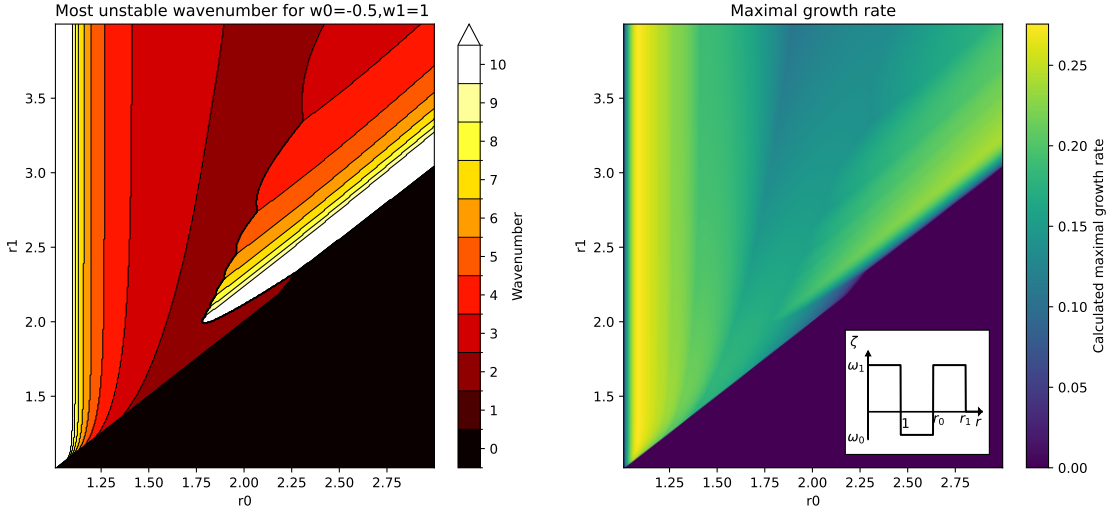

Figure 7. Instability for $\omega_0 = -0.5$ and $\omega_1 = 1$; left panel : most unstable wavenumber. right panel : growth rates. Insert: radial profile of mean vorticity.

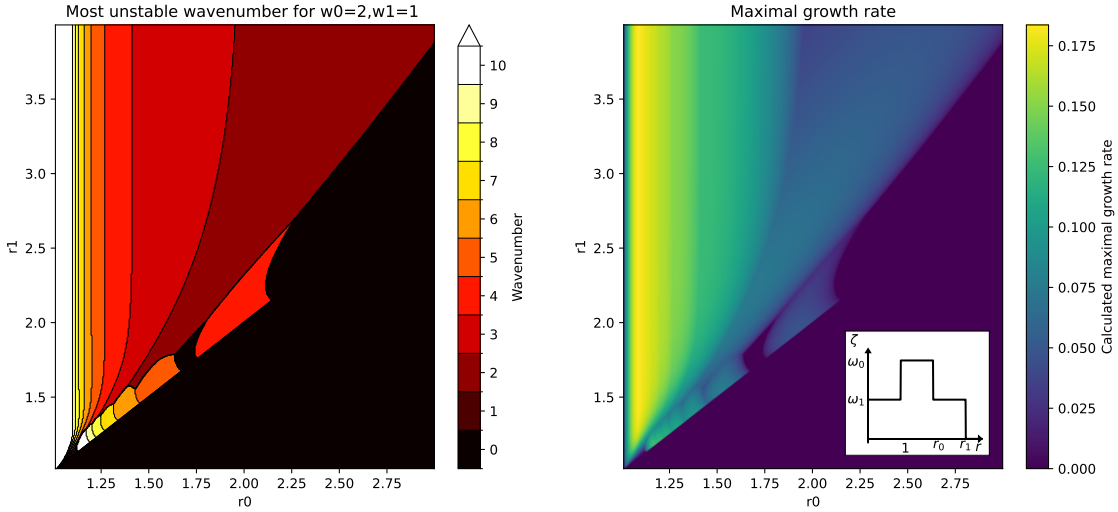

Figure 8. Instability for $\omega_0 = 2$ and $\omega_1 = 1$; left hand panel : unstable wavenumber. right panel : growth rates. Insert: radial profile of mean vorticity.

3.3.4. Case $\omega_0 = 2$, $\omega_1 = 1$

We now consider an opposite case, in which the trough vorticity $\omega_0 > 1$, with $\omega_1 < \omega_0$ (Fig. 8). Now only the Rossby waves on the inner and intermediate vorticity fronts can resonate. This is expected since they have opposite vorticity jumps, whereas the intermediate and outer fronts have like-signed jumps. Again, short unstable waves are favored when the fronts are close ($r_0 \simeq 1$), while longer waves are found for more distant fronts.

3.4. Linear instability of an annulus without core vortex

Referring to Reinaud and Dritschel (2019), we study the instability of a single annulus without central vorticity, i.e. $q_c = 0$ and $q_0 = 1$. The growth rates and most unstable waves are presented in figure (9). Both the growth rate and wave numbers depend on the difference between r_0

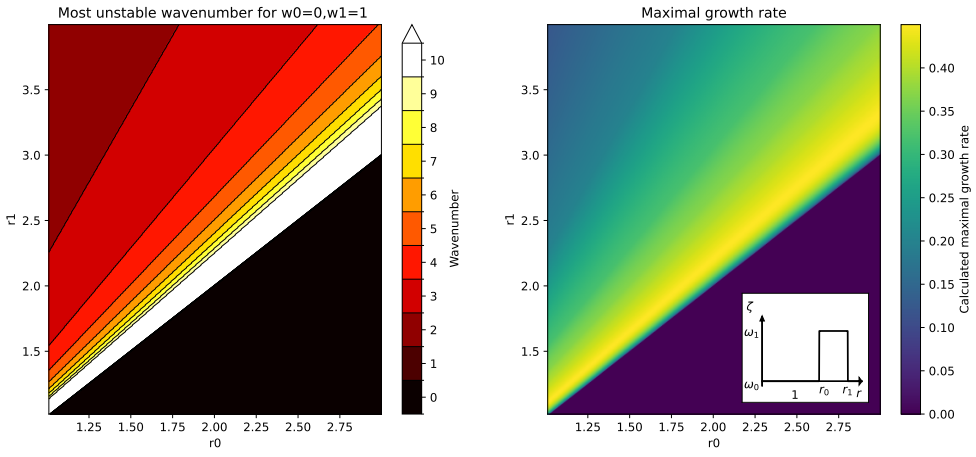

Figure 9. Instability of a vortex annulus with $\omega_0 = 1$; left : most unstable wavenumber. Right : growth rates. Insert: radial profile of mean vorticity

and r_1. Indeed, the closer the vorticity fronts, the more sensitive they are to Rossby wave resonance.

4. Nonlinear evolution of unstable vortices

Here, we study the nonlinear evolution of perturbed vortices using the code described in Section 2.3. Nonlinear evolutions for the cases **A** and **B**, previously studied in Section 3.2 (Figure 3) are shown in Figures 10 and 11, respectively.

4.1. Validation of the nonlinear growth rates compared to linear predictions

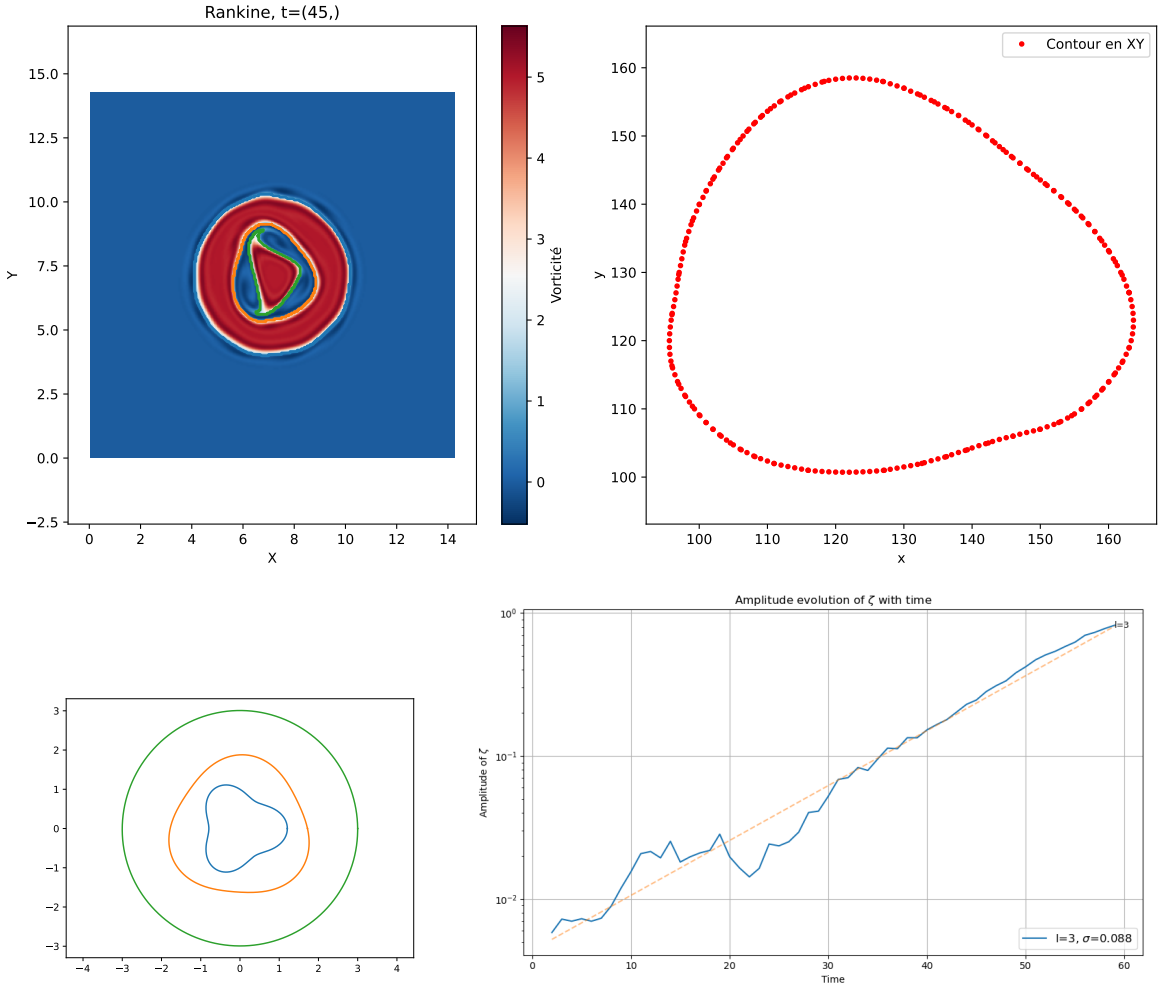

Figure 10. Case: $\omega_0 = 0, \omega_1 = 1, r_0 = 1.75, r_1 = 3.0$. Top: Vorticity map at time $t = 45$ of the nonlinear numerical model (left) and extraction of the intermediate contour (right). Bottom-left: most unstable (linear) eigenvector. Bottom-right: growth of the most unstable perturbation ($l = 3$, blue line) in the nonlinear model from the extracted contour, compared with the linear prediction (orange line).

We first compare the wave modes and growth rates of the most unstable modes, between the analytical (linear) calculation and the numerical (nonlinear) simulations (Figures 10 and 11). For case **A**, mode $l = 3$ is the most unstable in both cases. The analytical calculation yields a growth rate $\sigma \sim 0.09$, while the nonlinear simulation yields a value of $\sigma = 0.088$ for mode $l = 3$, which is very close to the analytical result (Fig. 10). For case **B**, the linear

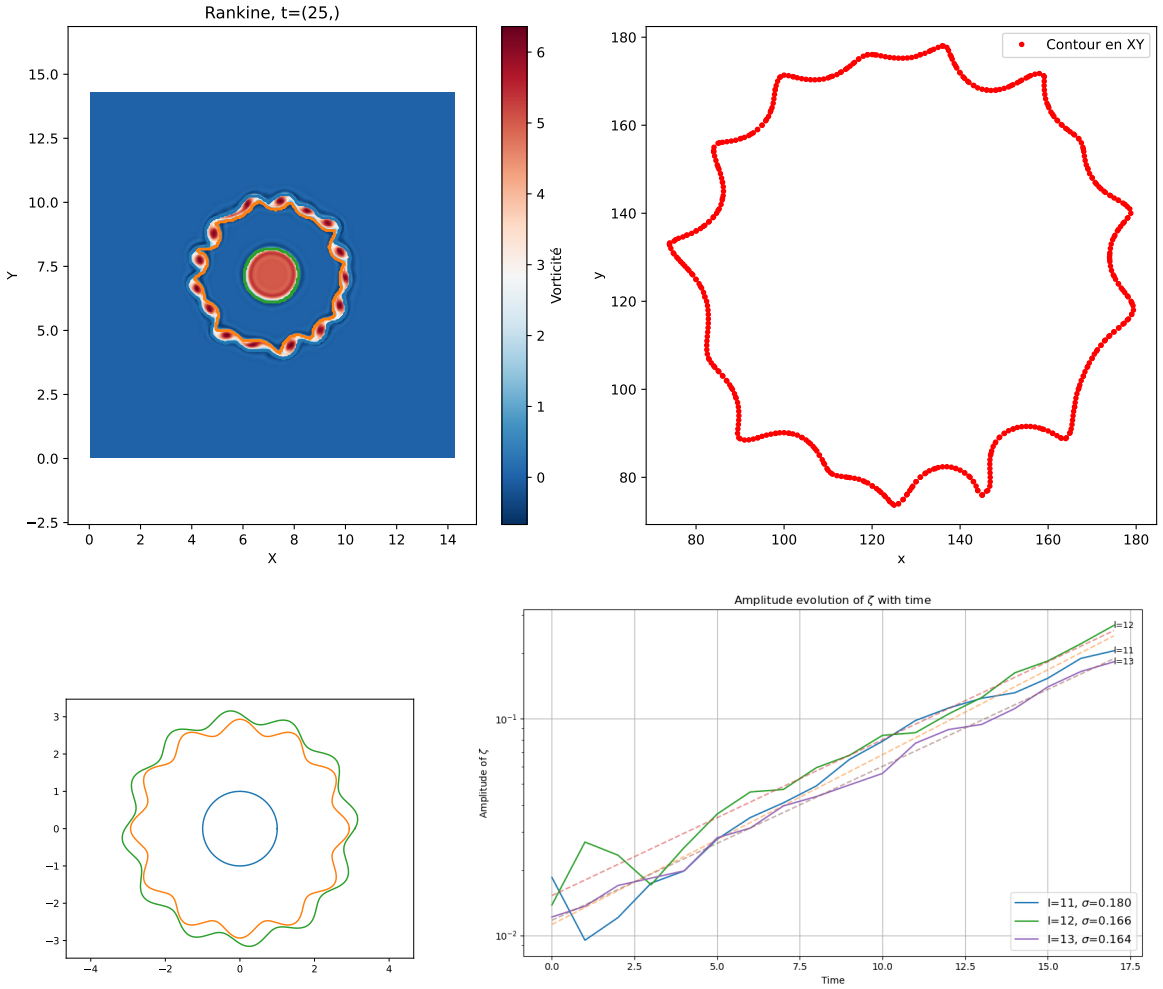

Figure 11. Case: $\omega_0 = 0, \omega_1 = 1, r_0 = 2.75, r_1 = 3.0$. Top: Vorticity map at time $t = 25$ of the nonlinear numerical model (left) and extraction of the intermediate contour (right). Bottom-left: most unstable (linear) eigenvector. Bottom-right: growth of the most unstable perturbations ($l = 11, 12, 13$) in the nonlinear model from the extracted contour, compared with the linear prediction (orange line).

calculation indicated that mode $l = 12$ is the most unstable, with a growth rate $\sigma \sim 0.155$. In the nonlinear simulation the three modes $l = 11, 12, 13$ have comparable growth rates (Fig. 11), with a growth rate of $\sigma = 0.166$ for mode $l = 12$. Differences between the linear and nonlinear values are smaller than 10%.

Both the linear and nonlinear models show the vorticity contours on which the eigenvectors are dominant. The inner and intermediate contours are dominant for case **A** (Fig. 10), and the intermediate and outer contours are dominant for case **B** (Fig. 11). It should also be noted that the numerical model growth rates are obtained via a linear regression (best fit) ; this calculation is sensitive to the time interval chosen. In particular, at early times, there may be a topological rearrangement of the initial perturbation towards the linearly most unstable mode (see for instance the green curve for mode $l = 12$ in Fig. 11).

4.2. Classification of nonlinear regimes

Different nonlinear evolutions can be observed depending on the values of r_0, r_1, ω_0, and ω_1. The nonlinear regimes are classified in the (r_0, r_1) plane for various values of ω_0 and ω_1. The main regimes (nonlinear evolutions) observed are:

(a) (**Quasi**) **stability** : stabilization of linearly unstable waves at finite amplitude, for which the vortex remains coherent for a long time
(b) **Core instability** : breaking of linearly unstable waves on the inner and intermediate contours, the outer contour remaining coherent
(c) **Ring instability** : breaking of linearly unstable waves on the intermediate and outer contours, the inner contour remaining coherent
(d) **Vortex breaking** : complete splitting of the whole vortex ; all unstable waves grow unbounded
(e) **Mixed instability** : Perturbations on both inner and outer contours, a mix between cases (b) and (c).

We can relate these main types of evolution to the physical parameters of the mean vortex: $r_0, r_1, \omega_0, \omega_1$.

Figure 13 presents the different nonlinear regimes of the linearly unstable vortex. Evolution (a) corresponds to the whole vortex undergoing little change in its outer contour and the inner vorticity rearranging on the dominant linear mode (l) (Fig. 12). Evolution (b) corresponds to the core breaking up into l fragments (Fig. 12). For r_1 close to r_0, instabilities affect mostly the vortex periphery, with the annulus breaking up into l independent vortices (Fig. 12); this corresponds to evolution (c). As soon as we make r_1 sufficiently close to r_0, an instability appears on the annulus. For certain values of r_1 larger than r_0 without being more than $1.5r_0$, a mixed instability can be observed: both on the core and on the ring. This corresponds to evolution (e).

When we allow for negative vorticity in the trough ($\omega_0 < 0, \omega_1 > 0$), the stability analysis shows the same unstable modes, but with a much larger growth rate (Fig. 7). This leads to very different nonlinear evolutions ending up in vortex breaking in most cases (Fig. 14). In the event of vortex breaking, the opposite vorticity poles rearrange and reassemble into dipoles, which then drift away (Fig. 12). For this configuration, we can only observe 'core instability' similar to that of the reference case when the intermediate contour is very close to the vortex core ($r_0 \approx 1$), i.e. when the mean vortex has little opposite-signed circulation in its central ring. In the configuration $r_0 = 1.25, r_1 = 3.5, \omega_0 = -1, \omega_1 = 1$, several unstable waves with different azimuthal modes l grow on the vortex rings ('Mixed instability'). The end-state is composed of several vorticity patches at the center of a vortex with unit vorticity (Fig. 12).

In the case with large vorticity in the annulus, $\omega_0 = 0, \omega_1 = 10$, we expect the most unstable modes to be short waves in the annulus, as per the stability analysis (Fig. 6). This is also what we observe with the nonlinear simulations, with the 'Ring instability' dominating in most cases (Fig. 15). The ring then breaks into l peripheral vortices in most cases. It is only for distant intermediate and outer vorticity contours ($r_0 = 1.25, r_1 \geq 3$) that the vortex is nonlinearly stable ('Quasi stability'). In this case, the initial unstable mode $l = 8$ decays into a mode $l = 6$ and then into a combination of modes $l = 2, 3$, finally generating (via nonlinear interaction), a mode $l = 1$ on the vortex contour, accompanied by small scale vorticity debris (Fig. 12). This shows that, during non-linear evolution, different modes can interact and transfer energy. This is detailed in the next subsection.

4.3. Mode interactions during the nonlinear evolution

Firstly, we analyze the evolution of the unstable circular vortex leading to ring instability, for which many perturbation waves grow to comparable amplitudes. This specific case corresponds to parameters $\omega_0 = 0, \omega_1 = 10, r_0 = 1.25, r_1 = 3$ considered in figure 15 (a quasi-stable evolution). With these parameters, the resonance occurs between the intermediate and the

(a) Formation of a triangular vortex with stabilizing waves on the vorticity contours ($\omega_0 = 3.0$, $\omega_1 = 2.0$, $r_0 = 2.25$, $r_1 = 2.6$)

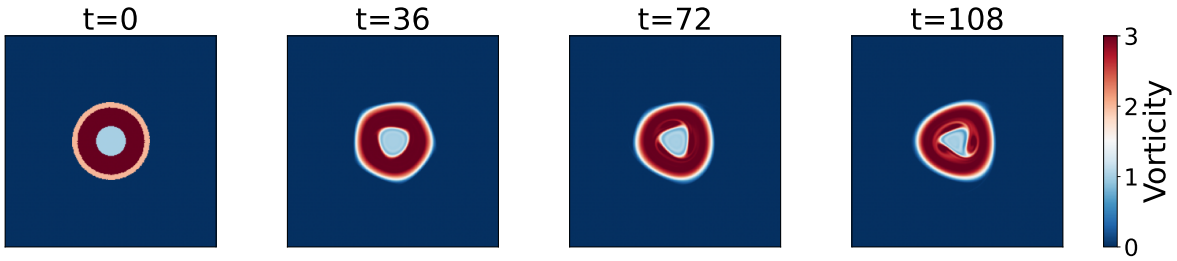

(b) Destruction of the core with a stable outer contour ($\omega_0 = 0.0$, $\omega_1 = 1.0$, $r_0 = 1.5$, $r_1 = 2.5$)

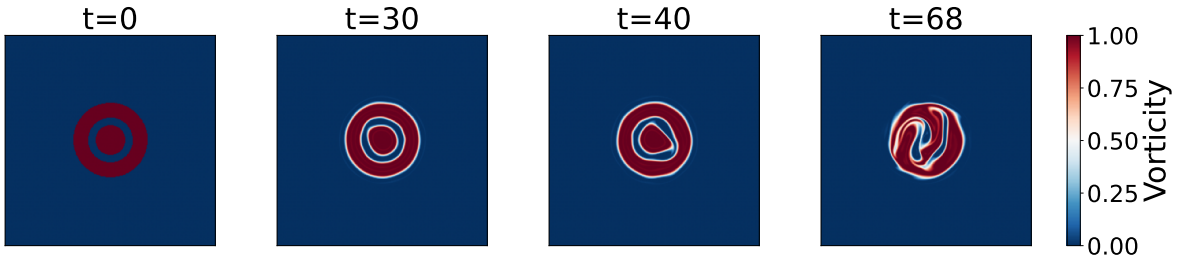

(c) Stable core with unstable vortex periphery leading to a multipole ($\omega_0 = 0.0$, $\omega_1 = 1.0$, $r_0 = 3.0$, $r_1 = 3.3$)

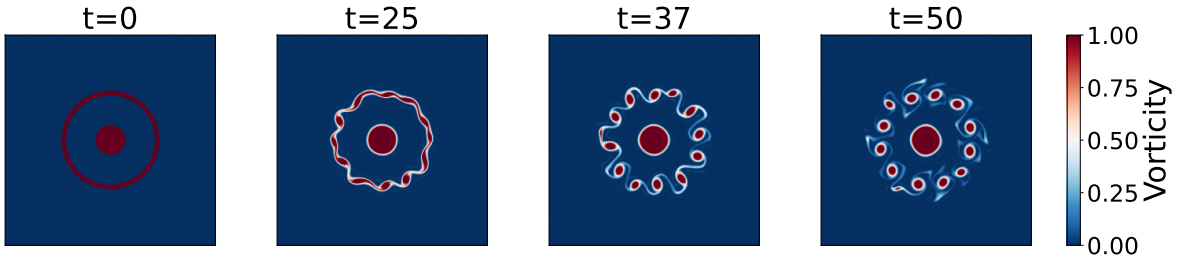

(d) Vortex breaking and outward motion of fragments ($a = 1.1$, $\omega_0 = \frac{1}{1-a^2}$, $\omega_1 = 0$, $r_0 = a$)

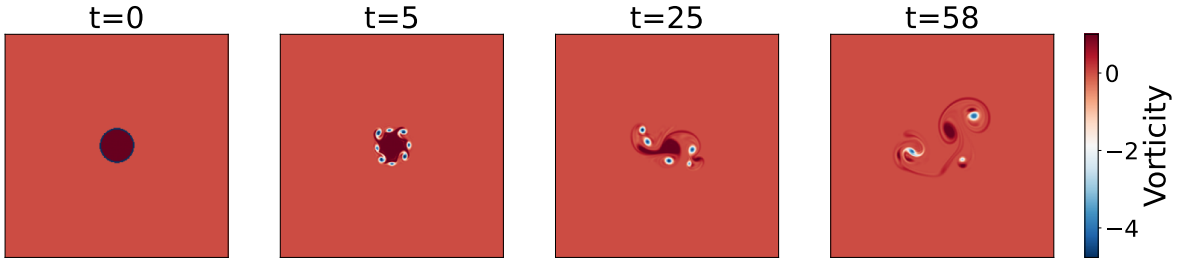

(e) Example of a mixed unstable vortex ($r_0 = 1.25$, $r_1 = 3.5$, $\omega_0 = -1$, $\omega_1 = 1$)

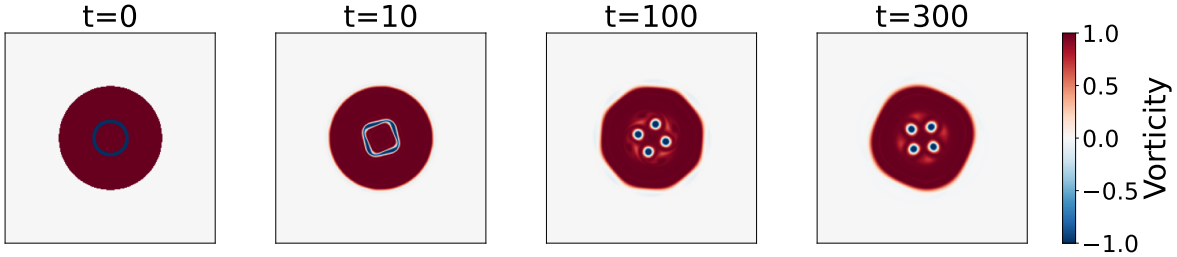

Figure 12. Vorticity fields showing different unwstable vortex evolutions simulated with the nonlinear numerical model: (a) (**Quasi**) **stability**, (b) **Core instability**, (c) **Ring instability**, (d) **Vortex breaking**, (e) **Mixed instability**.

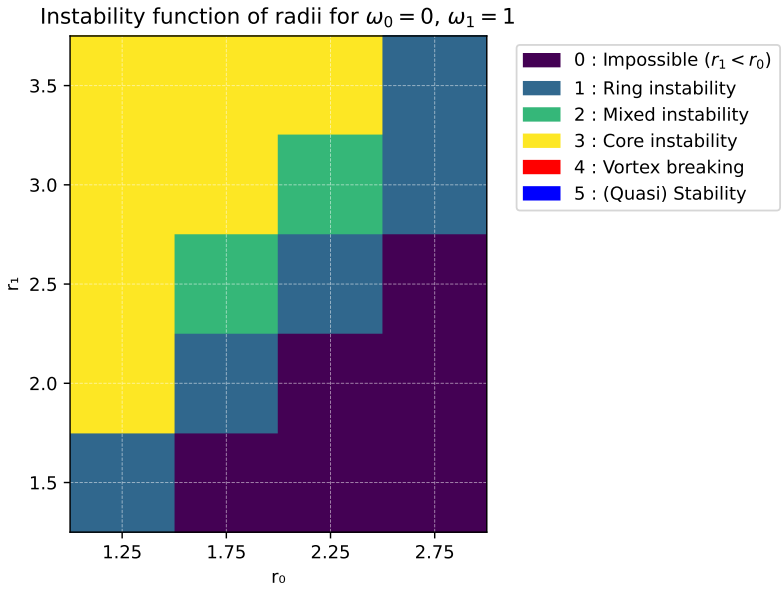

Figure 13. Nonlinear regimes of instability in the numerical model, for the reference case ($\omega_0 = 0.0, \omega_1 = 1.0$). The main evolutions affect either the vortex core, or its periphery.

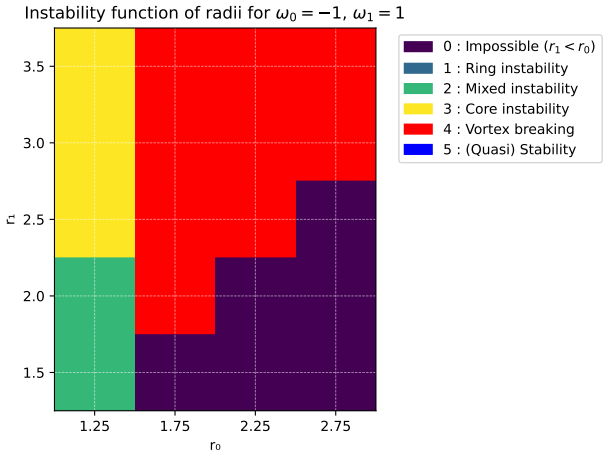

Figure 14. Nonlinear regimes of instability for $\omega_0 = -1$ and $\omega_1 = 1$; see previous caption for details.

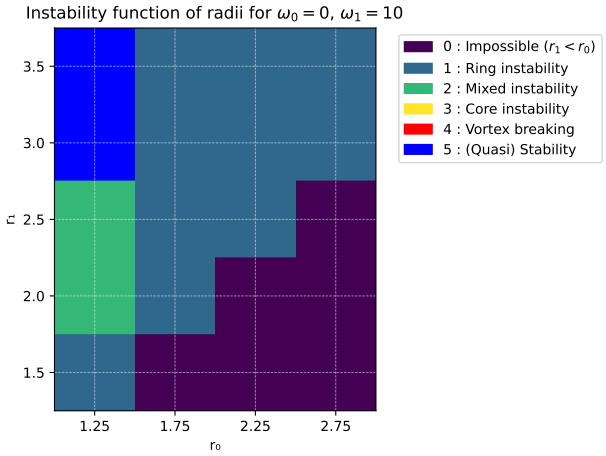

Figure 15. Nonlinear regimes of instability for $\omega_0 = 0$ and $\omega_1 = 10$; see previous caption for details.

outer vorticity fronts. Indeed, the angular Fourier analysis of the outer vorticity contour shows that mode $l = 8$ grows first, followed by mode $l = 6$ and subsequently by mode $l = 5$ on this front (and on the intermediate front, Fig. 16). In this case, several modes have comparable linear growth rates. This linear characteristic is reflected in the slope of the amplitude curves for the nonlinear simulation. The delay in the growth of modes 5 and 6 with respect to mode 8 may be due to the geometrical structure of the initial perturbation. The initial perturbation must be closer to the mode 8 eigenvector than to that of modes 5-6.

A second observation is that, as modes 5-6 grow, the amplitude of mode 8 decays. During this stage ($t = 10 - 30$), mode $l = 6$ prevails. This indicates an energy transfer between the former and the latter (via mode 2 of small amplitude). Finally, all modes $5 - 6 - 8$ reach a comparable amplitude, corresponding to the final stabilization of the vortex.

Next we investigate a different case that also leads to the formation of multipoles, namely

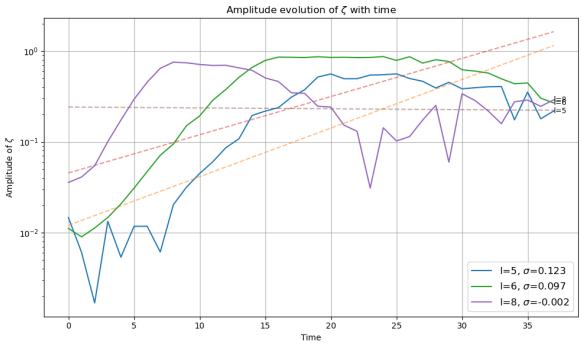

Figure 16. Fourier analysis of the case $\omega_0 = 0, \omega_1 = 10, r_0 = 1.25, r_1 = 3$

the one shown in the third row of figure 12. In this case, the vortex parameters are $\omega_0 = 0, \omega_1 = 1, r_0 = 3, r_1 = 3.3$. Its evolution is characterized as "ring instability" in the Table of figure 13. The Fourier angular mode analysis is presented in figure 17 : the nonlinear evolution shows that only mode $l = 10$ grows substantially. This mode is the most unstable one linearly and the nonlinear growth rate (close to 0.145 for $l = 10$) is close to the linear prediction (0.146 for $l = 9$). Now it is also clear that neither mode $l = 5$ (the subharmonic), nor modes $l = 15, 20$ (the various harmonics), grow substantially during the nonlinear evolution. Therefore, wave-wave interaction is weak in this case.

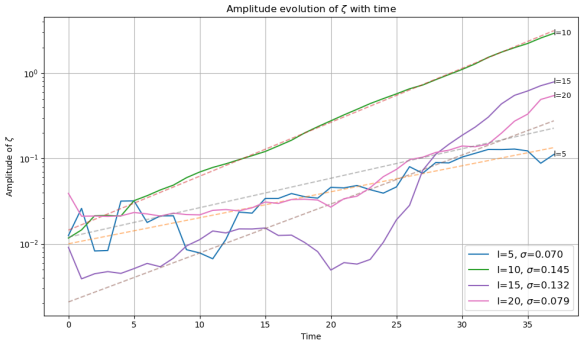

Figure 17. Fourier analysis of the case $\omega_0 = 0, \omega_1 = 1, r_0 = 3, r_1 = 3.3$

5. Multipole formation

We investigate here in more detail the formation of multipoles observed at the final stages of ring instabilities.

5.1. Observations of multipole formation

Detailed tables describing the nonlinear evolutions and final vortex states for various values of ω_0 and ω_1 are provided in appendix B. The cases $\omega_0 = -1, \omega_1 = 1$ and $\omega_0 = 0, \omega_1 = -0.1$ do not lead to the formation of multipoles with 5 or more satellites, but respectively to turbulence and to the formation of tripoles or of quadrupoles.

A few cases of multipole formation with many satellites (from 10 to 21) are observed for $\omega_0 = 0, \omega_1 = 1$, but many of them break and ultimately lead to a turbulent final state. Nevertheless, one case with 8 peripheral vortices is found for $r_0 = 4.9, r_1 = 5.5$. This

corresponds to satellite vortices much farther from the core than is observed at the North Pole of Jupiter.

For $\omega_0 = 0, \omega_1 = 10$, more multipoles are observed, with fewer satellites (5 to 9); for similarity with the polar vortices of Jupiter, a multipole with 8 satellites is formed for $r_0 = 1.8, r_1 = 2.0$ and $r_0 = 3.0, r_1 = 3.3$. Geometrically, this is close to the spatial observations. Nevertheless, physically, the condition $\omega_1 = 10$ does not apply to Jupiter (for which the core and satellite vortices have approximately the same velocity maximum at similar radii).

For $\omega_0 = -0.1$, $\omega_1 = 1$, we observe multipoles with 7 to 13 satellites which can degenerate in the long run. This underlines the stabilizing role of weak, opposite-signed vorticity between the core and the peripheral vortices. This inner ring of negative vorticity must not be too strong (e.g the $\omega_0 = -1\omega_1 = 1$ case) or else the vortex breaks irreversibly into small vortices and filaments (a turbulent field).

5.2. Stationary states of like-signed multipoles

Since the invariant integral method is not completely satisfactory, we look for steadily rotating steady states with $N = 8$ and $N = 5$ satellite vortices. We normalize the outer radius (r_1) to unity and define the two parameters $a = r_0/r_1$ and $b = 1/r_1$. Following the algebra by Morel and Carton (1994), we obtain analytical formulae for the shape of such multipoles (Fig. 18). These shapes are qualitatively similar to those obtained by a numerical steady state algorithm, and also identical to that used in Morel and Carton (1994). Peripheral vortices for $N = 5$ and $N = 8$ have slightly different shapes between the analytical and numerical results; this is explained by the hypotheses $\delta_a := \frac{r_a}{r_c} << 1$ and $\delta_b << 1$ used to compute the analytical steady states, while in the case presented here, $\delta_a \approx \delta_b \approx 0.3$. The numerical algorithm is more precise (up to second order in the small δ ratios) and should be considered as the reference. Note also that the steady states are close to the multipoles resulting from the instability of a circular vortex with the same parameters.

5.3. Stability of the stationary states

Firstly, we have used the multipolar state with $\omega_0 = 0.0, \omega_1 = 1.0$ and $r_0 = 5.0, r_1 = 7.0$ as an initial condition for the nonlinear model. We have perturbed it initially with a 1% white noise disturbance in vorticity. The simulation lasted 80 turnover periods. It showed only a slight vacillation of the vorticity contours, but no destabilization. The final multipole was very similar to the initial state, we can deduce that the vortex is stable on this long period.

Now, we propose a simple analytical criterion for the stability of multipoles. Considering that all vortices have like-signed vorticity, we consider the case where they have equal vorticity and radii (the simplest case). Then, it is known that two circular vortices merge if their initial distance is less than about 3.2 radii (or 3.3 depending on the calculus, see Melander *et al.* (1988) and Dritschel (1986)). This criterion can be applied to the interaction between two satellite vortices, or between one satellite and the core vortex.
Using the notation a, b above for the vortex boundaries, and assuming that $b = (1 - a)/2$, the center and satellites will not merge if $(1 + a)/2 > 3.2\ b = 3.2\ (1 - a)/2$, or roughly $b < 0.25$ and $a > 0.5$. This is indeed the case of the multipole shown here above.
Two satellites (among N) will not merge if their distance $d = 2\sin(\pi/N)\ (1 + a)/2 > 3.2\ (1 - a)/2$ or, with N large, $2\pi\ (1 + a)/N > 3.2\ (1 - a)$. This expression can be simplified into

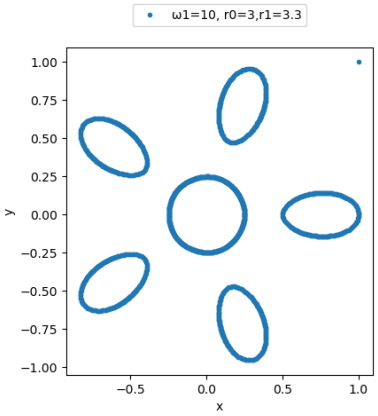

(a) Numerical steady state of a multipole for $N = 5$

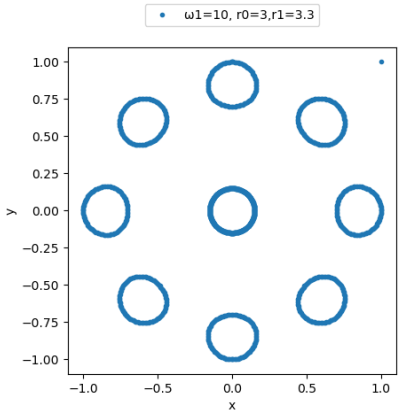

(b) Numerical steady multipole for $N = 8$

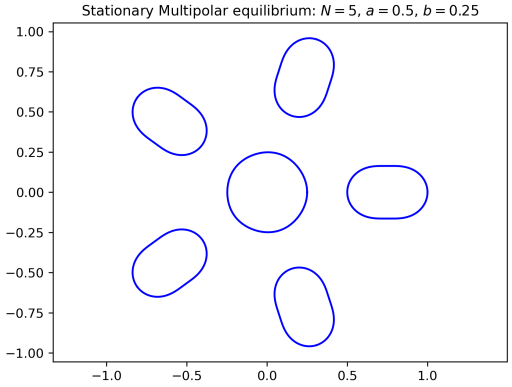

(c) Analytical steady multipole for $N = 5$

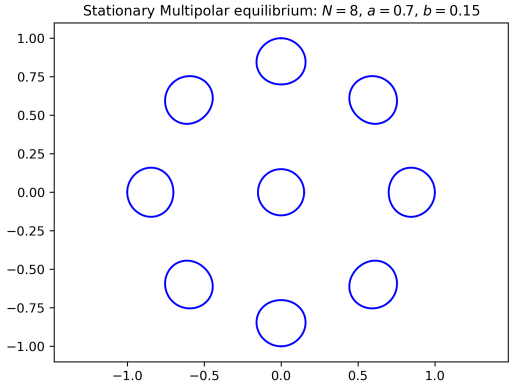

(d) Analytical steady multipole for $N = 8$

Figure 18. Comparison between analytical and numerical steady states for $N = 5$ and $N = 8$. For $N = 5$: $r_0 = 2$, $r_1 = 4$. For $N = 8$: $r_0 = 5.0$, $r_1 = 7.0$. Parameters: $\omega_0 = 0.0$, $\omega_1 = 1.0$.

$(1 + a)/(1 - a) > (3.2N)/(2\pi)$ $N/2$. With $N = 8$, we have $a > 0.6$, which is close to the limit of the previous paragraph. This is also verified by our stable multipole, studied numerically before.

6. Discussion and comparison to former studies

Firstly, we summarize the main findings of this study. Secondly, we compare them with the results of previous studies. Finally, we consider the specific cases of the Jupiter polar vortices.

6.1. Main results and specificity of the present study

Firstly, we have determined the linear instability characteristics (for normal modes) of the multi-front, like-signed vortices and we have characterized the dominant frontal wave resonance depending on $r_0, r_1, \omega_0, \omega_1$. We have considered analytically the cases that marginally satisfy the conditions for linear instability (see Appendix A).

For $\omega_0 = 0$, when $\omega_1 \approx 1$, wave resonance is controlled by the proximity of two among the three vorticity fronts. When two such fronts are very close, short waves can grow on them, while longer waves are more unstable when the fronts are distant. For large ω_1, the resonance is favored between the intermediate and outer vorticity waves. When $\omega_0 \neq 0$, the horizontal vorticity shear and the instability are increased for negative ω_0 and decreased when $\omega_0 \approx 1$.

Secondly, we have studied the nonlinear evolutions of the perturbed vortex. This has confirmed the linear theory predictions in terms of growth rates and spatial structure of the most unstable perturbation. The nonlinear evolutions has also shown the importance of wave-wave interaction in the development of the perturbation. More specifically,

- when a perturbation with a given wavenumber l is more unstable linearly than its neighbors ($l-1$ and $l+1$), this perturbation can grow nonlinearly and end up breaking, via the amplification of the harmonics of the initial wave. This leads in particular to the formation of the multipoles with a central vortex and several peripheral vortices. An example is shown on figure 12(c) with a short wave affecting mostly the vorticity annulus.
- when several perturbations with close wavenumbers $(l-1, l, l+1)$ have comparable growth rates, these waves interact and lead to a complex breaking of the initial vortex. This is the case shown in figure 12(b) where several waves break on the vortex core and intermediate vorticity contour, leading to the formation of asymmetric vortices at the center of the end-state.

The nonlinear evolution also yielded spatially confined end-states (for non-negative ω_0). This is explained by the absence, in these cases, of dipolar vortices that can drift away from the center of the plane. On the contrary, when $\omega_0 < 0$, such dipoles can be formed and expel vorticity outwards (see for instance, figure 12(d)).

Finally, we have shown instances of robust multipole formation, in particular with $N = 8$ satellites, and we have provided a simple analytical condition for their existence.

6.2. Comparison with previous studies of unstable shielded vortices

Imposing that all vorticity patches be like-signed makes a clear difference with former studies of vortex stability, when the multi-front vortices are (so-called) "shielded" or "neutral", that is, when they include an area with opposite-signed vorticity, or when their total circulation vanishes. In particular, our results for vortices with like-signed core and annulus, are very different from the two cases of :
- a two-contour shielded vortex (Carton *et al.* 1989) which often breaks into dipoles;
- a three-contour shielded vortex with zero total circulation (e.g. $\omega_0 = 0$ and $\omega_1 = 1/(r_0^2 - r_1^2)$), a case studied by Morel and Carton (1994), for which the multipoles formed are mostly transient for $l > 3$.

Now, we compare our results with those by Reinaud and Dritschel (2019), who studied the instability of a torus of uniform vorticity in a three-dimensional quasi-geostrophic model. In some instances, they added a sphere of vorticity at the center of the torus. Figure 19 compares the growth rates between our model and theirs. Their parameters can be related to ours via: $q_c = 1, q_0 = \omega_1$, $r_0 = (r_0 + r_1)/2$, their r_0 is our $(r_1 - r_0)/2$ and $\omega_0 = 0$. Though we can note minor differences, the comparison is fair between the most unstable modes and their growth rates in the two models, taking into account that in two dimensions, the vorticity fronts are closer to each other, than in three dimensions. Also in three dimensions, stratification tends to damp barotropic (horizontal shear) instability.

Concerning nonlinear evolutions, the study by Reinaud and Dritschel (2019) indicates that multipoles with $l = 4$ or $l = 5$ are stable, while they are unstable with $l = 3$ and $l \geq 6$ in the absence of a central spherical vortex, while the vortices with $l \geq 6$ are stabilized in its presence.

In figures 20,21,22 and 23, we can observe similarities and differences between our plots and

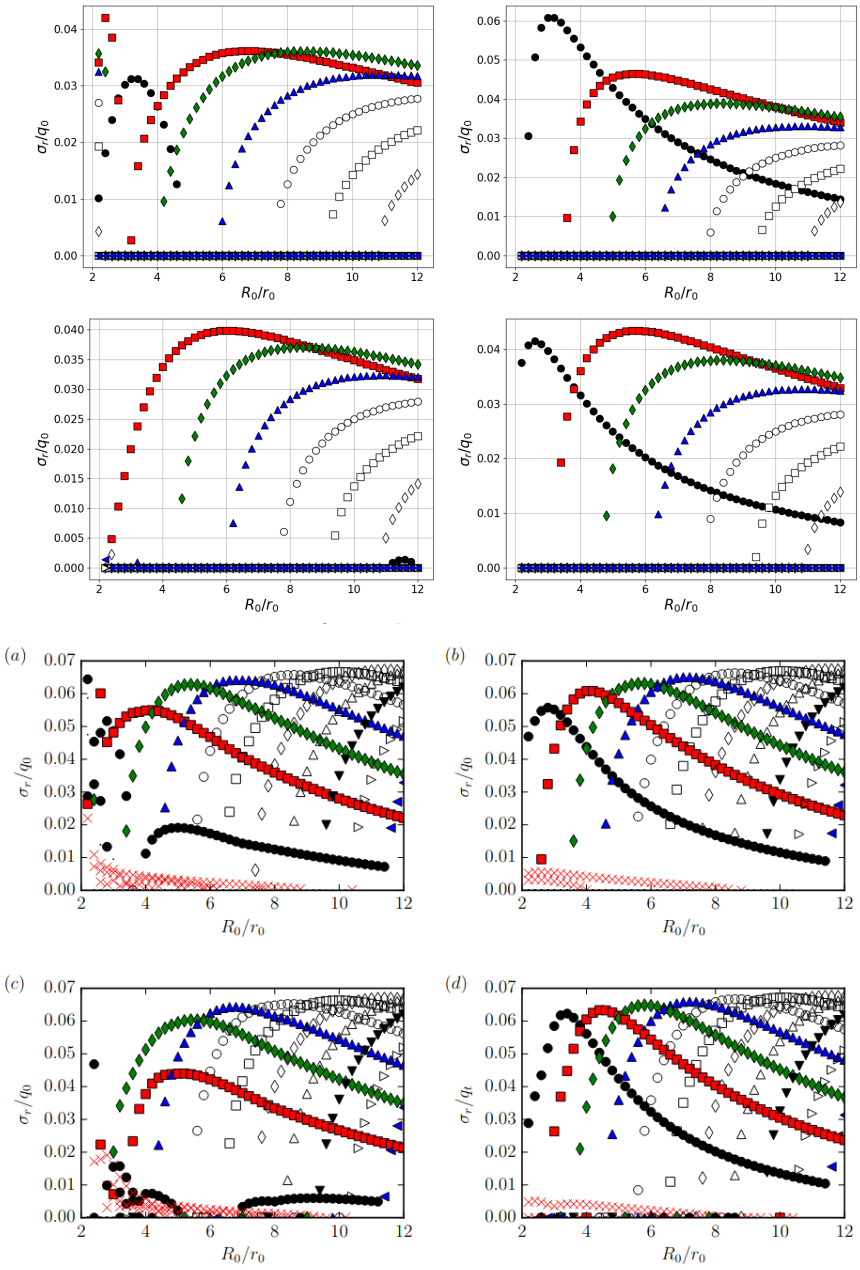

FIGURE 2. Growth rates σ_r of the unstable modes vs the torus normalised radius R_0/r_0 for $2.2 \leqslant R_0/r_0 \leqslant 12$, with $\Delta(R_0/r_0) = 0.2$, and for a central spherical vortex of radius $r_c = r_0$. The PV ratio between the central vortex and the torus is (*a*) $q_c/q_0 = 1$, (*b*) $q_c/q_0 = -1$, (*c*) $q_c/q_0 = 3$ and (*d*) $q_c/q_0 = -3$. Symbols indicate the azimuthal wave number of the mode: $m = 1\,\times$, $2\,\bullet$, $3\,\blacksquare$, $4\,\blacklozenge$, $5\,\blacktriangle$, $6\,\circ$, $7\,\square$, $8\,\lozenge$, $9\,\triangle$, $10\blacktriangledown$, $11\,\triangleright$, $12\,\blacktriangleleft$.

Figure 19. Comparison of the growth rates in our model (top) for $q_c/q_0 = 1$ (top left), $q_c/q_0 = -1$ (top right), $q_c/q_0 = 3$ (bottom left, $q_c/q_0 = -3$ (bottom right), with those in the toroidal vortex model of Reinaud and Dritschel (2019), their figure 2.

those of the article by Reinaud and Dritschel (2019):

- Unstable modes are not exactly the same (generally one order higher in our model, due to the closest boundaries mentioned earlier).
- If the growth rates are close in the two models for $r_0 = 2$, they are surprisingly very different for $r_0 = 4$. We cannot yet account for this difference.

- For $r_0 = 6$ the first mode is 5 but the system slowly evolves towards a four-vortex compound.

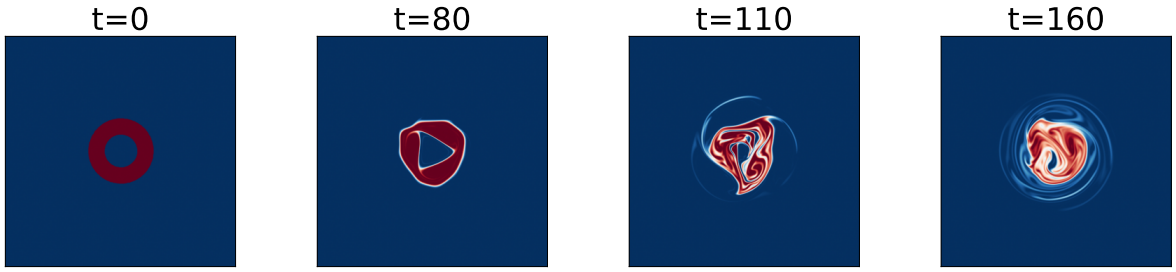

Figure 20. Time-series of 2D vorticity maps for an annulus with $r_0 = 2$

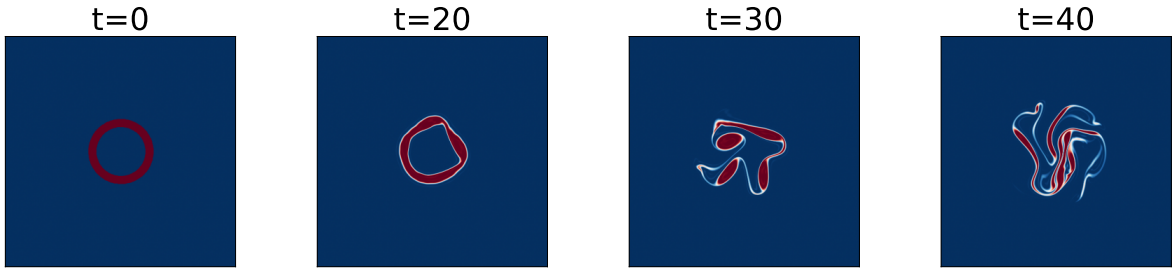

Figure 21. Time-series of 2D vorticity maps for an annulus with $r_0 = 4$

In particular, figure 22 shows a sequence of such transitions. The annulus evolves into a 6-vortex system, then a 5-vortex system, and, after many rotations, ends up as a 4-vortex association.

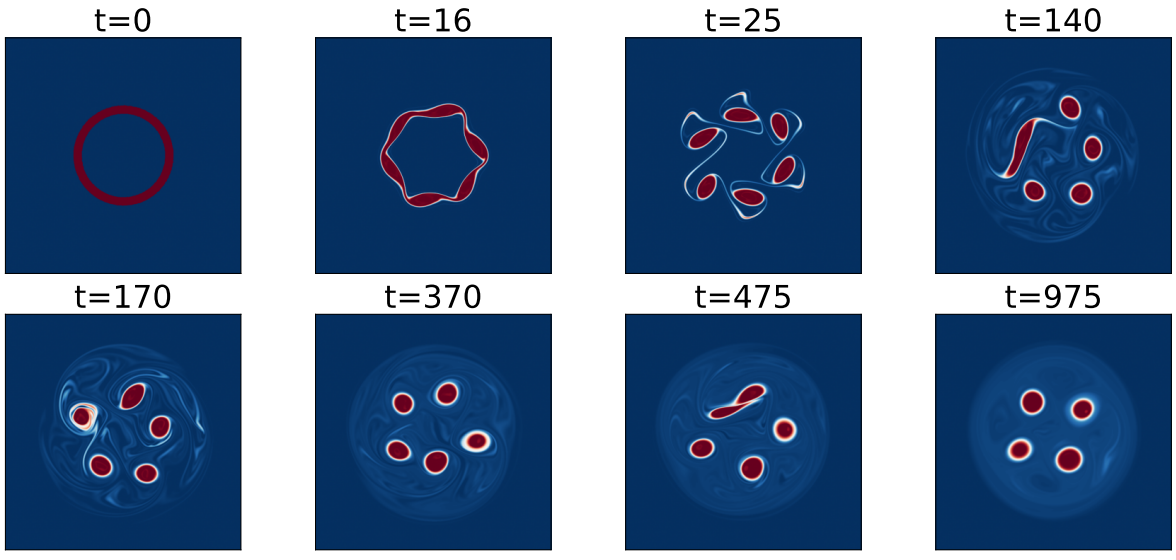

Figure 22. Time-series of 2D vorticity maps for an annulus with $r_0 = 6$.

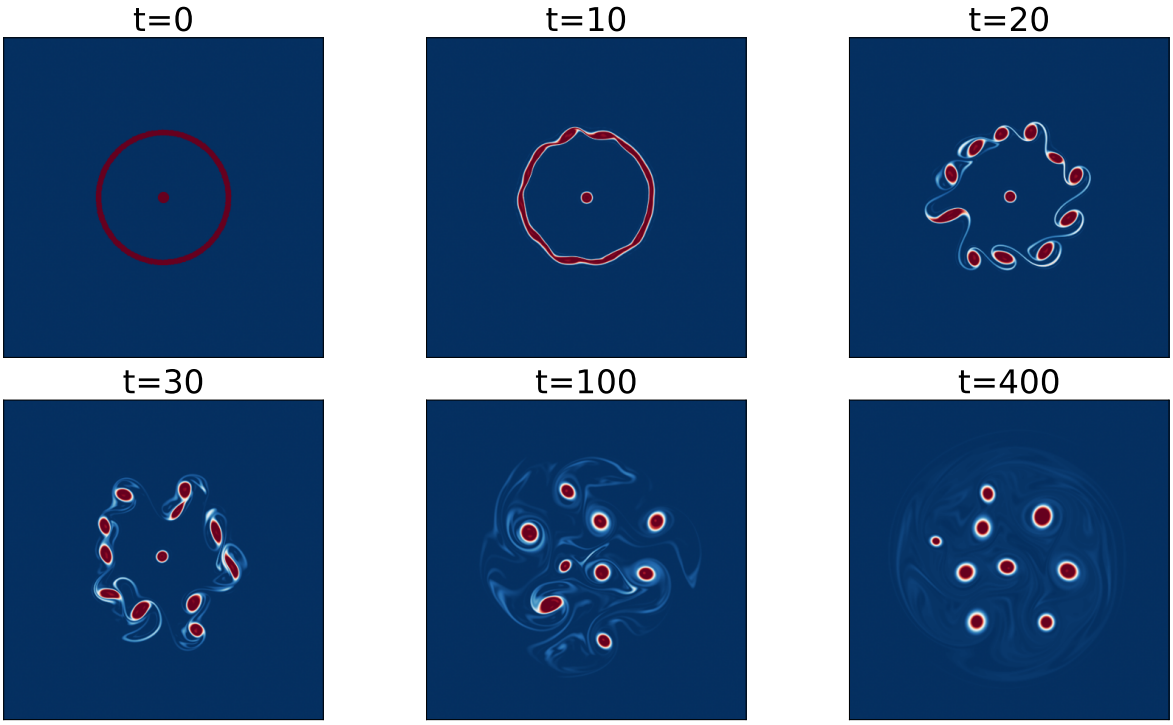

Figure 23. Time-series of 2D vorticity maps for an annulus with $r_0 = 12$ and $q_c/\omega_0 = 1$.

6.3. Comparison with space probe observations of the Jupiter polar vortices

From the data in Ingersoll *et al.* (2022), the radius of the central vortex at the North pole of Jupiter is 1000 km. Juno images show that all vortices around Jupiter's North pole have similar radii, and that the center of the peripheral vortices lies about 7000-8000 km from the pole. In our model, these values lead to $r_0 = 6.7$ and $r_1 = 8.7$.
The surrounding vorticity measured by Juno leads approximately to $\omega_0 = -0.075$ in our model, when $\omega_1 = 1$: with these parameters, the maximal growth rate is obtained for $l = 4$. This result is more appropriate to the South pole of Jupiter than to its North pole.
For a better agreement with the Juno observations, more ingredients should be added, in particular, a finite radius of deformation.
In Dritschel (2021), good works are also done modeling vortices around Jupiter's poles with a Point-vortex system.

7. Conclusions and openings

This study was originally motivated by the observations of vortex multipoles at the poles of Jupiter, but the very simple framework used here, allowing many analytical calculations, is not sufficient to explain the observations. Clearly, three dimensional effects come into play for Jupiter polar vortices. Still, a detailed knowledge of the internal structure of the Jupiter atmosphere, the exact 3D structure of the polar vortices and a fairly accurate value of this deformation radius, are not completely available. Recent studies mention values ranging from 250 km to 1500 km for R_d. This implies that an extension of our study to finite R_d has to take it into account as a supplementary parameter to be varied. This extension is under way, but will be the subject of a forthcoming paper. Without providing details, it is known that, with a finite R_d, the external velocity fields of vorticity patches decay exponentially rather than inversely, with r. This will damp the instability of circular vortices with distant core and

annuli. As a consequence this will favor the growth of perturbations with high wavenumbers when the vorticity fronts are close to each other. Then, the instability of vortex multipoles will also be diminished.

This extension to a more complex framework is necessary to convincingly present circular vortex instability as an alternative to vortex aggregation, for the formation of the multipoles at the Jupiter poles. Even more complex frameworks can include horizontal variations of temperature (as in the thermal quasi-geostrophic model), or vertical stratification. But again, more data will be necessary to adequately fit the model parameters to precise values.

Acknowledgements

The first author thanks Ecole Normale Superieure de Rennes for a Ph.D grant; all authors are grateful to UBO for support during the course of this study.

Appendix A: Asymptotic cases of linear instability; analytical study

For barotropic instability to occur, the Rayleigh criterion must be satisfied, following Rayleigh (1895). Here, we investigate analytically the vorticity profiles that marginally satisfy the Rayleigh criterion. To this aim, we expand the matrix A in ϵ, the difference in ω_0, ω_1 between a stable state according to the Rayleigh criterion and a possibly unstable state. Below, we study two simple cases :

A.1. Case with a small outer vorticity : $\omega_0 = 0$, $\omega_1 = \varepsilon$

In this case, approximations give

$$A = \frac{1}{2l}\begin{pmatrix} l-1 & r_0^{1-l}\varepsilon & -r_1^{1-l}\varepsilon \\ -r_0^{-l-1} & \frac{l}{r_0^2}+\varepsilon & -(\frac{r_0}{r_1})^{l-1}\varepsilon \\ -\frac{1}{r_1^{l+1}} & (\frac{r_0}{r_1})^{l+1}\varepsilon & \frac{l}{r_1^2}+\varepsilon(l-1+\frac{l}{r_1^2}). \end{pmatrix} \tag{A.1}$$

The equation obeyed by $\mu = 2lc$ is the following one, after canceling terms in ε of order > 2 :

$$\begin{aligned}(\tau-\mu)\left((\tau+1)\rho-\mu\right)\left((\tau+1)\xi-\mu\right) \\ +\varepsilon\left[\left(\rho^l+\tau-\mu\right)\left((\tau+1)\xi-\mu\right)+\left(-\xi^l+\tau-\mu\right)\left((\tau+1)\rho-\mu\right)\right]=0,\end{aligned} \tag{A.2}$$

with $\tau = l-1, \rho = 1/r_0^2, \xi = 1/r_1^2$.

When $\varepsilon = 0$, the eigenvalues are the diagonal terms : $\mu_0 = \tau, \mu_1 = (\tau+1)\rho, \mu_2 = (\tau+1)\xi$. All the roots are simple and different ($l-1 \geq 1 > \frac{1}{r_0^2} > \frac{1}{r_1^2}$ or $l-1 = 0 \neq \frac{1}{r_i}$), and by continuity of the roots, the polynomial still has real roots for ε small enough : the system is stable for ε small enough.
This indicates that the Rayleigh criterion for instability is necessary, but not sufficient.

A.2. Case with a small intermediate vorticity : $\omega_0 = 1+\varepsilon$, $\omega_1 = 1$

In this case, approximations give

$$A = \frac{1}{2l}\begin{pmatrix} l+\varepsilon & -\varepsilon r_0^{1-l} & -r_1^{1-l} \\ \frac{1}{r_0^{l+1}}\varepsilon & l+\varepsilon(l-\frac{l}{r_0^2}-1) & -(\frac{r_0}{r_1})^{l-1} \\ \frac{1}{r_1^{l+1}}\varepsilon & -(\frac{r_0}{r_1})^{l+1}\varepsilon & l-1+\frac{l\varepsilon}{r_1^2}(r_0^2-1). \end{pmatrix} \tag{A.3}$$

Here again for $\varepsilon = 0$ any normal mode is linearly stable on the vortex.
When the matrix is approximated at first order in ε, several terms are canceled in the determinant. Then, μ must satisfy the following equation :

$$(l-\mu)^2(l-\mu-1) + \varepsilon\left[\frac{1-r_0^{2l}}{r_1^{2l}}(l-\mu)+ \right.$$
$$\left.(l-\mu)(l-1-\mu) + (l-\mu)(l-1-\mu)\left(l-\frac{l}{r_0^2}-1\right) + \frac{l(l-\mu)^2(r_0^2-1)}{r_1^2}\right] = 0. \tag{A.4}$$

Setting $x := l-\mu$ we obtain the equation :

$$x\left[x(x-1)+\varepsilon\left(\frac{1-r_0^{2l}}{r_1^{2l}} + (x-1)\left(l-\frac{l}{r_0^2}\right) + \frac{l}{r_1^2}x(r_0^2-1)\right)\right] = 0, \tag{A.5}$$

for which $\mu = l$ is an eigenvalue.
Let us denote :

- $\alpha := \frac{l(r_0^2-1)}{r_0^2}$,
- $\beta = \frac{1-r_0^{2l}}{r_1^{2l}}$,
- $\gamma = \frac{l(r_0^2-1)}{r_1^2}$,

then, the equation becomes then

$$x^2 + [\varepsilon(\alpha+\gamma)-1]\,x + \varepsilon(\beta-\alpha) = 0 \tag{A.6}$$

In this case, the equation has a double root for $\varepsilon = 0$; this renders the evolution unpredictable without calculating higher orders than unity. To illustrate this problem, consider the equation $x^2+\varepsilon x+\varepsilon^2 = 0$; it has real roots 0 and $-\varepsilon$ at $O(\varepsilon)$. But it has complex roots whose imaginary part is proportional to ε when considered at $O(\varepsilon^2)$.

Numerically we observe that the instability depends on r_0 and r_1. Most often, when this vortex is unstable, the growth rate is proportional to ε, but stability was found for $r_1 = 2.5$ and $r_0 \geq 2.1774$.

Appendix B: Detailed tables of nonlinear evolutions of unstable vortices, and of final vortex states

In this appendix, we provide more detailed tables than figures 13, 14, 15 for the final vortex states, after the nonlinear evolution of the linearly unstable circular vortices. Using a large number of numerical simulations, we can identify in which case, vortex multipoles can form, and in particular, vortices with 5 or more satellites, as observed at the poles of Jupiter.

For $q_c = 1.0, \omega_0 = -1.0, \omega_1 = 1.0$ (not shown), most nonlinear evolutions are strongly irreversible, leading to filamentation, a disordered array of vortices or turbulence.

r_1 \ r_0	1.3	1.5	2	2.5	3	3.5	4	5	6
1.6	M4C/CV+Tu	—	—	—	—	—	—	—	—
1.8	—	1CV+3PV	—	—	—	—	—	—	—
2	M4C/1CV+Tu	M3C/Brk	—	—	—	—	—	—	—
2.2	—	—	FiPc→Fi+Tu/Axisym	—	—	—	—	—	—
2.5	M4C/1CV+M6P	M3C/Brk	FiPV/Tu	—	—	—	—	—	—
2.7	—	—	—	15PV/Brk	—	—	—	—	—
2.8	—	—	—	12PV/Brk	—	—	—	—	—
3	M5C/1CV+M7P	M4C/Brk	—	FiPV/Tu	—	—	—	—	—
3.1	—	—	—	—	21PV/Brk	—	—	—	—
3.3	—	—	—	—	11PV	—	—	—	—
3.4	—	—	—	—	Brk	—	—	—	—
3.8	—	—	—	—	—	10PV	—	—	—
4	M4C/1CV+M4P	M4C/Brk	—	—	—	M4P/Tu	—	—	—
4.5	—	—	—	—	—	—	M4P/Tu	—	—
5	M4C/CV brk	M4C/Brk	—	—	—	—	—	—	—
5.5	—	—	—	—	—	—	—	8PV	
6.5	—	—	—	—	—	—	—	—	12PV/Tu
7	—	—	—	—	—	—	—	—	4PV/Tu

Table B1. Nonlinear evolutions and final vortex states - under the form (NE/FVS) - for $\omega_c = 1.0, \omega_0 = 0, \omega_1 = 1.0$

r_1 \ r_0	1.3	1.5	1.8	2	2.5	3	3.5	4	5
1.6	M5C/Fi	—	—	—	—	—	—	—	—
1.8	—	M4C/6PV	—	—	—	—	—	—	—
2	M4C/Tu	M4C/Axisym	1CV+8PV	—	—	—	—	—	—
2.2	—	—	—	10PV/Me	—	—	—	—	—
2.5	M3C/Brk	M3C/Axisym	—	4PV/Axisym+Tu	—	—	—	—	—
2.7	—	—	—	—	10PV→Me	—	—	—	—
2.8	—	—	—	—	7PV	—	—	—	—
3	M3C/Tu	M3C/Tu	—	—	1CV+3PV	—	—	—	—
3.1	—	—	—	—	—	1CV+9PV	—	—	—
3.3	—	—	—	—	—	1CV+8PV	—	—	—
3.4	—	—	—	—	—	7PV	—	—	—
3.8	—	—	—	—	—	—	Tu	—	—
4	—	M3C/Tu	—	—	—	—	*M4P/Tu*	—	—
4.5	—	—	—	—	—	—	—	1CV+6PV	—
5	—	—	—	—	—	—	—	—	—
5.5	—	—	—	—	—	—	—	—	1CV+4PV

Table B2. Nonlinear evolutions and final vortex states - under the form (NE/FVS) - for $\omega_c = 1.0, \omega_0 = 0, \omega_1 = 10.0$

r_1 \ r_0	1.3	1.5	2.5	3	3.5	4
1.6	M4C/Tu	—	—	—	—	—
1.8	—	3PV+T	—	—	—	—
2	M4C/Tu	3M+T	—	—	—	—
2.5	M4C/1CV	1CV	—	—	—	—
2.7	—	—	1CV+Fi	—	—	—
2.8	—	—	1CV+Fi	—	—	—
3.0	M4C/1 CV	—	1CV+Tu	—	—	—
3.1	—	—	—	1CV+13PV	—	—
3.3	—	—	—	1CV+10PV	—	—
3.4	—	—	—	1CV+8PV	—	—
3.8	—	—	—	—	1CV+10PV	—
4.0	MC4C/1CV	—	—	—	1CV+7CV	—
4.5	—	—	—	—	—	1CV+9PV
5.0	M4C4/1CV	—	—	—	—	PV Brk

Table B3. Nonlinear evolutions and final vortex states - under the form (NE/FVS) - for $q_c = 1.0, \omega_0 = -0.1, \omega_1 = 1.0$

For $q_c = 1.0, \omega_0 = 0, \omega_1 = -0.1$ (a shielded vortex, table not shown here), most evolutions yield final tripolar or quadrupolar vortices, as it has been reported in the literature.

CV	Central Vortex	nPV	n Peripheral Vortices
MnP	Mode n perturbation on vortex periphery	MnC	Mode n perturbation on central vortex
Brk	Vortex breaking	Tu	Turbulence
Fi	Vortex filamentation	Axisym	Vortex axisymetrization

Table B4. Table of acronyms for the final vortex states

	Core Breaking : regular final state
	Core Breaking : irregular final state
	Peripheral Breaking : regular multipole formation
	Peripheral breaking : peripheral turbulence and irregularity
	General vortex breaking / unbounded evolution

Table B5. * Color code for vortex evolutions

References

Antuñano, A., del Río-Gaztelurrutia, T., Sánchez-Lavega, A., Read, P.L. and Fletcher, L.N., Potential vorticity of Saturn's polar regions: Seasonality and instabilities. *Journal of Geophysical Research: Planets*, 2019, **124**, 186–201.

Baey, J. and Carton, X., Vortex multipoles in two-layer rotating shallow-water flows. *Journal of Fluid Mechanics*, 2002, **460**, 151–175.

Carli, E., Morrow, R., Vergara, O., Chevrier, R. and Renault, L., Ocean 2D eddy energy fluxes from small mesoscale processes with SWOT. *Ocean Science*, 2023, **19**, 1413–1435.

Carton, X., Hydrodynamical Modeling Of Oceanic Vortices. *Surveys in Geophysics*, 2001, **22**, 179–263.

Carton, X., Flierl, G. and Polvani, L., The generation of tripoles from unstable axisymmetric isolated vortex structures. *Europhys. Lett.*, 1989, **9**, 339–344.

Carton, X. and McWilliams, J., Barotropic and baroclinic instabilities of axisymmetric vortices in a QG model. In *Mesoscale/Synoptic Coherent Structures in Geophysical Turbulence*, edited by J. Nihoul and B. Jamart, Vol. 50, pp. 225–244, 1989 (Elsevier Oceanographic Series: ????).

Carton, X. and McWilliams, J., Nonlinear oscillatory evolution of a baroclinically unstable geostrophic vortex. *Dynamics of Atmospheres and Oceans*, 1996, **24**, 207–214.

Cassini, J.D., A more particular account of those observations about Jupiter that were mentioned in numb. 8, Philosophical Transactions of the Royal Society of London 1666.

Clerke, A.M., *A popular history of astronomy during the Nineteenth Century*, 2nd edn, 1887 (Adam and Charles Black).

Corréard, S.M. and Carton, X.J., Formation and stability of tripolar vortices in stratified geostrophic flows. *Il Nuovo Cimento, C*, 1999, **22**, 767–777.

Dewar, W. and Killworth, P., On the Stability of Oceanic Rings. *Journal of Physical Oceanography*, 1995, **25**, 1467–1487.

Dewar, W., Killworth, P. and Blundell, J., Primitive-Equation Instability of Wide Oceanic Rings. Part II: Numerical Studies of Ring Stability. *Journal of Physical Oceanography*, 1999, **29**, 1744–1758.

Dritschel, D.G., The nonlinear evolution of rotating configurations of uniform vorticity. *Journal of Fluid Mechanics*, 1986, **172**, 157–182.

Dritschel, D.G., On the stabilization of a two-dimensional vortex strip by adverse shear. *Journal of Fluid Mechanics*, 1989, **206**, 193–221.

Dritschel, D.G., Scott, R.K. and Reinaud, J.N., The stability stability of quasi-geostrophic ellipsoidal vortices. *Journal of Fluid Mechanics*, 2005, **536**, 401–421.

Dritschel, D., Ring configurations of point vortices in polar atmospheres. *Regular and Chaotic Dynamics*, 2021, **26**, 467–481.

Dritschel, D., Nonlinear stability bounds for inviscid, two-dimensional, parallel or circular flows, with monotonic vorticity, and the analogous three-dimensional quasi-geostrophic flows. *J. Fluid Mech.*, 1988, **191**, 575–581.

Dritschel, D. and De la Torre Juárez, M., The instability of tall columnar vortices in a quasi-geostrophic fluid. *J. Fluid Mech.*, 1996, **328**, 129–160.

Flierl, G., On the instability of geostrophic vortices. *J. Fluid Mech.*, 1988, **197**, 349–388.

Ford, R., The instability of an axisymmetric vortex with monotonic potential vorticity in rotating shallow water. *J. Fluid Mech.*, 1994, **280**, 303–334.

Gavriel, N. and Kaspi, Y., The number and location of Jupiter's circumpolar cyclones explained by vorticity dynamics. *Nature Geoscience*, 2021, **14**, 559–563.

Gent, P. and McWilliams, J., The instability of barotropic circular vortices. *Geophys. Astrophys. Fluid Dyn.*, 1986, **35**, 209–233.

Godfrey, D., A hexagonal feature around Saturn's north pole. *Icarus*, 1988, **76**, 335–356.

Hogg, N.G. and Stommel, H.M., The heton, an elementary interaction between discrete baroclinic geostrophic vortices, and its implications concerning eddy heat-flow. *Proceedings Royal Society London A*, 1985, **397**, 1—-20.

Hua, B., The internal barotropic instability of surface-intensified eddies. Part I. Generalized theory for isolated eddies. *J. Phys. Oceanogr.*, 1988a, **18**, 40–55.

Hua, B., The internal barotropic instability of surface-intensified eddies. Part II. Modeling of the Tourbillon site. *J. Phys. Oceanogr.*, 1988b, **18**, 56–71.

Ingersoll, A., Ewald, S., Tosi, F. *et al.*, Vorticity and divergence at scales down to 200 km within and around the polar cyclones of Jupiter. *Nature Astronomy*, 2022, **6**, 1280–1286.

Kurakin, L.G., Ostrovskaya, I.V. and Sokolovskiy, M.A., On the stability of discrete tripole, quadrupole, Thomson' vortex triangle and square in a two-layer/homogeneous rotating fluid. *Regul. Chaot. Dyn.*, 2016, **21**, 291–334.

Li, C., Ingersoll, A., Klipfel, A. and Brettle, H., Modeling the stability of polygonal patterns of vortices at the poles of Jupiter as revealed by the Juno spacecraft. *Proceedings of the National Academy of Sciences of the U.S.A.*, 2020, **117**, 24082–24087.

McWilliams, J.C., Geostrophic Vortices, Lecture Notes for the Varenna Summer School (Enrico Fermi International School of Physics) 1991.

Melander, M.V., Zabusky, N.J. and Mcwilliams, J.C., Symmetric vortex merger in two dimensions: causes and conditions. *Journal of Fluid Mechanics*, 1988, **195**, 303–340.

Morel, Y. and Carton, X., Multipolar vortices in two-dimensional incompressible flows. *J. Fluid Mech.*, 1994, **267**, 23–51.

Rayleigh, On the stability or instability of certain fluid motions (iii.). *Proceedings of the London Mathematical Society*, 1895, **1**, 5–12.

Reinaud, J.N., Three-dimensional quasi-geostrophic vortex equilibria with m-fold symmetry. *Journal of Fluid Mechanics*, 2019, **863**, 32–59.

Reinaud, J.N. and Dritschel, D.G., The stability and nonlinear evolution of quasi-geostrophic toroidal vortices. *Journal of Fluid Mechanics*, 2019, **863**, 60–78.

Richardson, P.L. and Tychensky, A., Meddy trajectories in the Canary Basin measured during the SEMAPHORE experiment, 1993–1995. *Journal of Geophysical Research*, 1998, **103**, 25029–25045.

Rostami, M., Zeitlin, V. and Spiga, A., On the dynamical nature of Saturn's North Polar hexagon. *Icarus*, 2017, **297**, 59–70.

Roullet, G., Fluid2d: A versatile Python–Fortran CFD code for 2D flows, GitHub repository Version consultée le May 18, 2026 2025.

Sanchez-Lavega, A., Lecacheux, J., Colas, F. and Laques, P., Ground-Based Observations of Saturn's North Polar Spot and Hexagon. *Science*, 1993, **260**, 329–332.

Scarica, P., Grassi, D., Mura, A., Adriani, A., Ingersoll, A., Li, C., Piccioni, G., Sindoni, G., Moriconi, M.L., Plainaki, C., Altieri, F., Cicchetti, A., Dinelli, B.M., Filacchione, G., Migliorini, A., Noschese, R., Sordini, R., Stefani, S., Tosi, F. and Turrini, D., Stability of the Jupiter Southern Polar Vortices Inspected Through Vorticity Using Juno/JIRAM Data. *Journal of Geophysical Research: Planets*, 2022, **127**, e2021JE007159.

Siegelman, I., Young, W. and Ingersoll, A., Polar vortex crystals: Emergence and structure. *Proceedings of the National Academy of Sciences of the U.S.A.*, 2022, **119**, e2120486119.

Sokolovskiy, M., Stability of an Axisymmetric Three-Layer Vortex. *Izvestiya Atmospheric and Oceanic Physics*, 1997, **33**, 16–26.

Sokolovskiy, M.A. and Carton, X.J., Baroclinic multipole formation from heton interaction. *Fluid Dyn. Res.*, 2010, **42**, 045501.

Sokolovskiy, M.A. and Verron, J., Finite-core hetons: stability and interactions. *Journal of Fluid Mechanics*, 2000, **423**, 127—-154.

Svedhem, H., Titov, D., McCoy, D., Lebreton, J.P., Barabash, S., Bertaux, J.L., Drossart, P., Formisano, V., Häusler, B., Korablev, O., Markiewicz, W., Nevejans, D., Pätzold, M., Piccioni, G., Zhang, T., Taylor, F., Lellouch, E., Koschny, D., Witasse, O., Eggel, H., Warhaut, M., Accomazzo, A., Rodriguez-Canabal, J., Fabrega, J., Schirmann, T., Clochet, A. and Coradini, M., Venus Express–The first European mission to Venus. *Planetary and Space Science*, 2007, **55**, 1636–1652.

Sánchez-Lavega, A., del Río-Gaztelurrutia, T., Hueso, R., Pérez-Hoyos, S., García-Melendo, E., Antuñano, A., Mendikoa, I., Rojas, J.F., Lillo, J., Barrado-Navascués, D., Gomez-Forrellad, J.M., Go, C., Peach, D., Barry, T., Milika, D.P., Nicholas, P. and Wesley, A., The long-term steady motion of Saturn's hexagon and the stability of its enclosed jet stream under seasonal changes. *Geophysical Research Letters*, 2014, **41**, 1425–1431.